DynamicPrint: A Physics-guided Feedforward Model Predictive Process Control Approach for Defect Mitigation in Laser Powder Bed Fusion Additive Manufacturing

Alex Riensche[*1,2], Benjamin Bevans[1,2], Antonio Carrington[2], Kaustubh Deshmukh[2],
Kamden Shephard[2], John Sions[3], Kyle Snyder[3], Yuri Plotnikov[3], Kevin Cole[4], Prahalada Rao[2,4]

[1]Industrial and Systems Engineering, University of Oklahoma, Norman, OK, USA
[2]Grado Department of Industrial and Systems Engineering, Virginia Tech, Blacksburg, VA, USA
[3]Commonwealth Center for Advanced Manufacturing, Disputanta, VA, USA
[4]Mechanical and Materials Engineering, University of Nebraska-Lincoln, Lincoln, NE, USA
[5]Mechanical Engineering, Virginia Tech, Blacksburg, VA, USA
[*]Corresponding Author, email: ariensche@ou.edu; ariesnche@vt.edu.

Abstract

In this work, we developed and applied a physics-guided autonomous model process control approach called *DynamicPrint* to mitigate defects in laser powder bed fusion (LPBF) additive manufacturing. Currently, the processing parameters for LPBF of a specific material are optimized through empirical testing of simple-shaped coupons. These optimized parameters are typically maintained constant when printing complex parts. However, using constant parameters often causes uneven temperature distribution in complex parts, leading to such defects as inhomogeneous microstructure, poor surface finish, thermal-induced distortion, and build failures. By contrast, DynamicPrint autonomously adjusts the processing parameters layer-by-layer before an LPBF part is printed to prevent non-uniform temperature distribution and mitigate thermal-induced defects. The *a priori* process parameter adjustments in DynamicPrint are guided by rapid physics-based thermal simulations. Through experiments with complex stainless steel 316L LPBF parts, we demonstrate the following beneficial outcomes of DynamicPrint: (i) homogenous grain sizes and consistent properties (microhardness); (ii) improved geometric accuracy and surface integrity of hard-to-access internal features; and (iii) avoidance of recoater crashes and elimination of supports in parts with prominent overhang features. DynamicPrint can greatly accelerate the time-to-market for LPBF parts by offering a rapid, physics-based method for process qualification, unlike the current cumbersome and expensive empirical build-and-test approach.

Keywords: Laser Powder Bed Fusion (LPBF), Thermal History, Physics-based Feedforward Process Control, Model Predictive Control, SS 316L.

1 Introduction

1.1 Objective and Motivation

This work concerns the laser powder bed fusion (LPBF) additive manufacturing process (Figure 1). The objective is to develop and apply a physics-based control approach termed *DynamicPrint* to autonomously adjust the processing parameters layer-by-layer for LPBF manufactured parts before they are printed. DynamicPrint, which is an embodiment of model predictive feedforward control, uses *a priori* validated physics-based thermal simulations to mitigate deleterious temperature trends that can cause defect formation in LPBF parts [1, 2]. DynamicPrint can potentially accelerate the time-to-market of LPBF parts by restraining the need for extensive build-and-test empirical studies toward process qualification.

The LPBF process is advantageous for manufacturing complex, high-value components which are difficult to create with traditional subtractive and formative techniques. As shown in recent industry case studies, the process enables significant reduction in manufacturing lead times, simplifies manufacturing by reducing the part count, and mitigates waste [3]. For example, recently, NASA successfully tested a rotating detonation engine with LPBF-manufactured fuel injectors that can potentially improve specific impulse up to 15% over existing rocket engines [4, 5]. Despite the capabilities of LPBF, adoption of the technology in safety-critical industries has been limited. A key barrier is the tendency of the process to produce flaws, such as porosity, distortion, and heterogenous microstructure [6]. These flaws, which are difficult to correct with post-process machining or heat treatment, can cause considerable variation in surface finish, geometric accuracy, mechanical properties, among other, leading to uncertainty in functional integrity of the part [7-10].

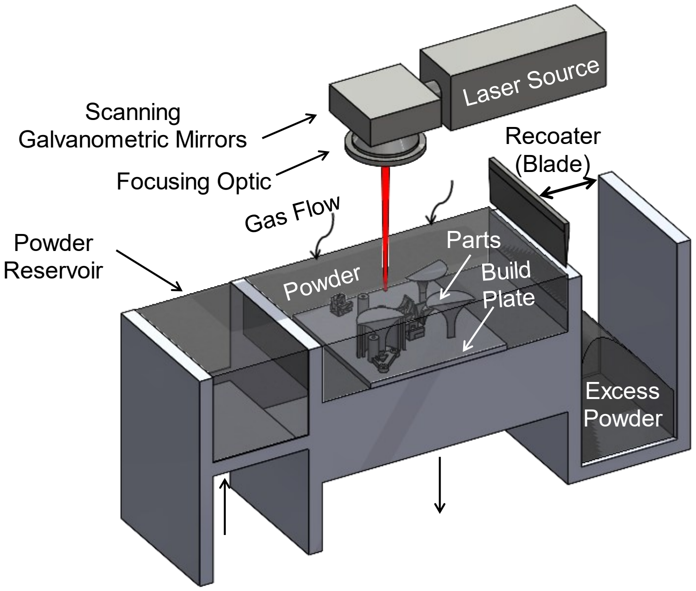

Figure 1: Schematic of the laser powder bed fusion (LPBF) process.

Flaw formation and inconsistent part properties are principally driven by the spatiotemporal temperature distribution in the part during the printing process [11]. The spatiotemporal temperature distribution, also called the thermal history, is governed by a large number of factors, such as part geometry, time between layers, orientation, support placement, processing parameters, and material selection, among others [12-14]. Due to the complex physical relationships underpinning these factors, the processing parameters and build conditions for a specific part shape are currently optimized through an empirical build-and-test approach [15, 16].

Researchers have noted that processing parameters optimized based on empirical testing of simple cuboid shapes seldom transfer to complex shapes [17]. Thus, further rounds of build-and-test iterations are frequently required to adjust the processing parameters to specific part shapes and build orientations. Indeed, Mohr *et al.* [17] recently reported that the processing window and part characteristics shift significantly when parameters optimized based on test cubes were used to produce relatively complex parts. This is because, thermal history of complex parts is not constant, but changes between layers of the same part. Some features, such as thin walls and overhangs, retain more heat than others [2, 18]. As a consequence of this uneven temperature distribution, microstructure characteristics, such as grain size and microhardness often vary between different sections of the part [19].

To illustrate, Figure 2 shows an LPBF-produced stainless steel 316L impeller [20]. The part was manufactured under *a priori* optimized processing conditions suggested by the powder manufacturer. The processing parameters were maintained constant throughout the build. Thermal simulations predicted that the fins of the impeller tend to overheat due to their narrow cross-section compared to its base. This uneven temperature distribution caused conspicuous anisotropy in the grain texture and orientation, as well as the occurrence of lack-of-fusion porosity as evident from electron backscatter diffraction imaging [20].

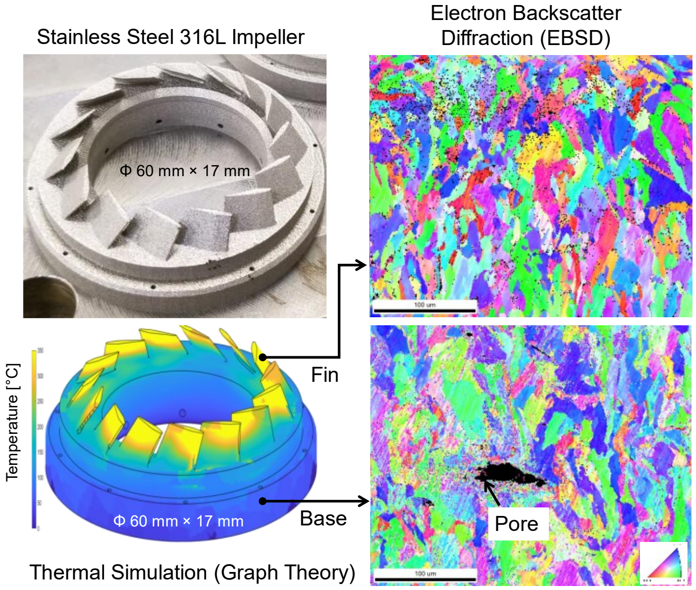

Figure 2: Manufacturing a complex LPBF part under constant processing conditions causes uneven temperature distribution, which in turn results in anisotropy and flaw formation as evident in the difference between the base in fin sections of the impeller part [20].

Since functional qualification of a practical part is predicated on extensive materials characterization and testing, it is estimated that the repetitive, empirical-reliant legacy approach to qualify the process for every new part often requires several years and costs millions of dollars

[21]. The qualification processes must be repeated if the part design or the build conditions are changed [22, 23]. The physics-based thermal simulation and control theory integrated DynamicPrint approach developed in this work, summarized in the following section (Sec. 1.2), has the potential to accelerate process qualification, and mitigate the cost and time needed for empirical studies.

1.2 Approach, Novelty, and Limitations

This work presents a physics-based approach to autonomously control the thermal history, and consequently mitigate flaw formation in LPBF parts, and overcome the expense and lack of transferability associated with empirically optimized LPBF processing conditions. The key idea behind DynamicPrint is to integrate predictions from a computational thermal simulation with a process control approach called model predictive control (MPC). Modeling and control are considered among the highest priority needs for realizing the potential of LPBF [24].

We emphasize that the aim of DynamicPrint is process control in LPBF. This aim is distinctive from offline process optimization based on design of experiments. Starting with part shape, material properties and manufacturer-recommended processing parameters, DynamicPrint autonomously adjusts the parameters layer-by-layer before the LPBF part is printed such that the predicted thermal history of the part matches a user-identified ideal thermal history. Subsequently, the controller-recommended process parameters are implemented by the slicing software of the LPBF machine (EOS Build) by the operator. DyamicPrint is therefore an embodiment of model predictive feedforward control; no changes to the processing parameters are made during the printing process through feedback control.

The DynamicPrint approach presented in this work is a significant departure from the current build-and-test methodology that prescribes maintaining processing parameters constant throughout all layers regardless of the geometry of the part. Indeed, to the best of our knowledge, it is one of the first works in physics-guided control in LPBF which autonomously produces a layer-by-layer process plan for an entire part customized to its shape and build orientation before it is printed. A summary of existing process control approaches in LPBF is provided in Sec. 2. The approach has the unique ability to achieve a desired thermal history by employing rapid graph theory-based computational thermal modeling.

Through experiments with different part shapes followed by comprehensive materials characterization, we demonstrate the following advantages from using the physics-based DynamicPrint approach: (i) reduction in microstructure heterogeneity resulting in consistent part properties, namely microhardness; (ii) improvement in geometric accuracy and surface integrity of hard to access internal features; and (iii) elimination of recoater crash and supports in parts with prominent overhang features. This work thus provides an avenue for rapid and shape agnostic LPBF process qualification based on thermal physics, as opposed to cumbersome empirical optimization.

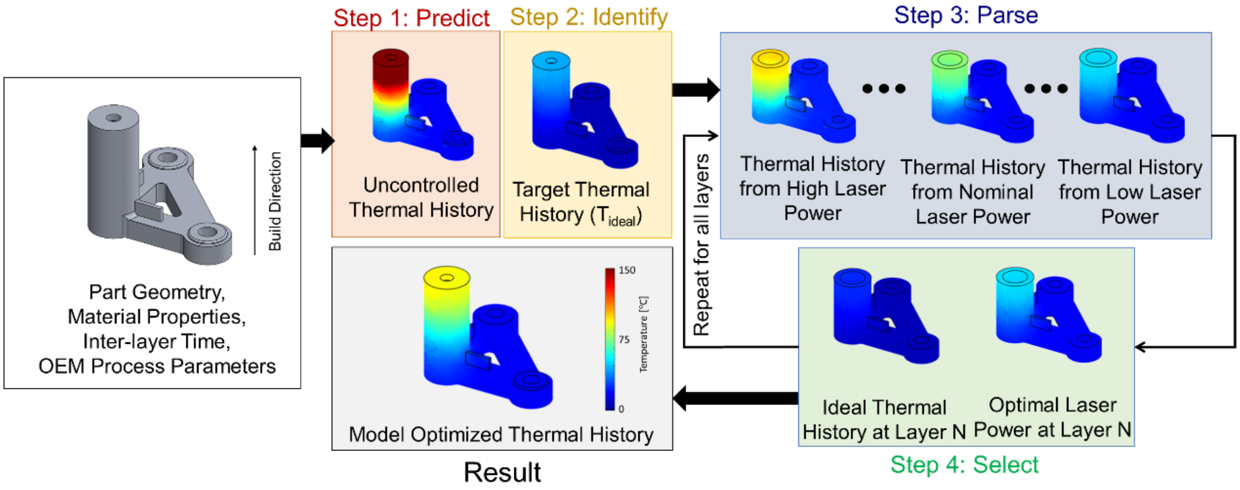

Figure 3: Overview of the model predictive control (MPC) DynamicPrint approach employed in this work to autonomously identify optimal LPBF process parameters before the part is built. Shown here is an example of a complex bell crank geometry in order to control end-of-cycle part temperature. The approach has four steps: (1) Predict, (2) Identify, (3) Parse, and (4) Select. Steps 3 and 4 are iterative.

The DynamicPrint approach consists of four steps as summarized in Figure 3. These four steps are labeled as: (1) Predict, (2) Identify, (3) Parse, and (4) Select, and are briefly described herewith.

- Step 1 (Predict): Given a part geometry, orientation, materials properties, starting processing conditions suggested by the manufacturer and boundary heat transfer conditions, the thermal history of the part is predicted using a rapid and meshless, graph theory-based thermal simulation model developed in our previous work [2, 19, 25]. Figure 3 exemplifies a complex bell crank shape whose model-predicted thermal history depicts heat accumulation and large variation in temperature between layers when printed under default manufacturer recommended conditions.
- Step 2 (Identify): In the predicted thermal history of the part from Step 1, deleterious thermal trends, such as overheating, are demarcated, and the ideal or target thermal history ($\widehat{\mathrm{T}}_{\mathrm{ideal}}$) devoid of such undesirable trends is identified. For the bell crank, an ideal thermal history was identified as one devoid of large temperature variations and having a uniform thermal history.
- Step 3 (Parse): The thermal history of the part for a select number of future layers is predicted using the graph theory thermal model with different process parameter inputs, such as changing laser power levels. Constraints motivated from practice are placed on the bounds of the processing parameters. In this work, only the laser power was adjusted, and every simulation epoch consists of five future layers. To avoid keyhole porosity and lack-of-fusion, the laser power is constrained to five discrete levels between 225 W and 146 W, respectively.
- Step 4 (Select): Pick those processing parameters from Step 3 that result in the closest match with the corresponding layers for the ideal thermal history ($\widehat{\mathrm{T}}_{\mathrm{ideal}}$) identified in Step 2.

Steps 3 and 4, which constitute together the core concept of DynamicPrint, are repeated iteratively for the whole part [26]. Thus, DynamicPrint entails iterative optimization of the thermal history at each simulation epoch. The outcome is a layer-by-layer process plan for a part, such that the predicted thermal history of the part closely matches a pre-determined ideal thermal history ($\widehat{\mathrm{T}}_{\mathrm{ideal}}$). The approach thus autonomously adjusts the process parameters layer-by-layer before the part is printed such that the model-predicted thermal history of a part matches a predetermined ideal or target thermal history. In this context, we clarify that the thermal history was controlled at the layer-level and not at discrete individual material points. The specific thermal history control metric is called average end-of-cycle temperature (T_{e}), viz., the average steady state temperature of a layer after it is melted. Whilst the DynamicPrint approach can be readily scaled for controlling the thermal history at discrete, individual material points, the commercial LPBF machine used in this work prevents point-wise process parameter control. As depicted in Figure 3, it is not possible for the final thermal history to match exactly the ideal thermal history in practice due to constraints placed on the adjustable levels of processing parameters.

The most computationally demanding aspect of DynamicPrint is in Step 3 (Parse), where the thermal history is estimated as a function of different process parameter levels. Further, the control schema is iterative in nature as it repeats Steps 3 and 4 at each simulation epoch. Physics-based model predictive control (MPC) approaches, akin to DynamicPrint, for autonomous LPBF process optimization have not been implemented because iterative prediction of the thermal history using existing finite element (FE) based modeling is computationally demanding [27]. The key enabler of DynamicPrint is the meshless graph theory approach for prediction of thermal history used in this work which is an order of magnitude faster than FE modeling [2, 18]. Although commercial FE-based solutions for thermal modeling can drastically reduce the computation time compared to research-level FE solutions, they do not currently incorporate the ability to autonomously prescribe adjustment of parameters to compensate for potential heat retention [28]. To overcome these limitations, researchers are actively developing rapid modeling techniques, including surrogate models, and leveraging GPU-accelerated FE simulations [22, 29-32].

A limitation of the DynamicPrint approach is that only one processing parameter, the laser power, is adjusted. Whilst, apart from laser power, other key process input variables, such as the laser velocity, hatch spacing, and layer height could be adjusted within both the model and LPBF machine, these are not attempted due to the computational complexity associated with adjusting multiple variables simultaneously within a controller. Adjustment of laser velocity is not adopted because increasing the velocity to decrease heat retention is liable to create meltpool instability and spatter [33]. Moreover, increasing the laser velocity also reduces the time between layers, which exacerbates heat retention. On the other hand, reducing the laser velocity is liable to increase the processing time and cause keyhole porosity [33]. Changing of layer height would be time inefficient and error prone as it requires mechanical positioning of the powder bed. Lastly, increasing hatch spacing to decrease heat retention may cause poor consolidation of tracks within a layer, resulting in lack-of-fusion porosity [34]. In other words, adjusting the laser power offers both the most rapid and practically viable approach for control of thermal history without sacrificing process stability and efficiency. Thus, adjusting the laser power offers both the most rapid and practically viable approach for control of thermal history without sacrificing process stability and efficiency (time).

Note on difference from the authors' prior work. In one of our previous published works, we implemented a feedforward control approach for LPBF which involved changing the laser power and inter-layer dwell time between layers [18]. In this prior work, described in Ref. [18], we demonstrated that changing the laser power and increasing the dwell time between layers to mitigate heat accumulation resulted in consistent microstructure and improvement in geometric resolution compared to parts built under constant processing conditions. However, this previous work has the following two significant limitations which are remedied by the model predictive control DynamicPrint approach presented in the current work. First, in our prior work there was no target or ideal thermal history, i.e., there is no Identify Step 2 in Figure 3. The aim of the prior work was to only mitigate the large-scale heat buildup. Therefore, unlike DynamicPrint, the prior heuristic feedforward approach was unable to control the thermal history to a specific desired or target trend. Second, the parameter adjustments (laser power and dwell time) to mitigate heat accumulation were based purely on operator intuition and several hours of manual, trial-and-error simulations. By contrast, the DynamicPrint approach is autonomously adjusts the process parameters. Lastly, in DynamicPrint only the laser power was adjusted, the dwell time was not adjusted because it increases the processing time and diminishes productivity.

The rest of this paper is organized as follows. In the forthcoming Sec. 2, we briefly review the existing literature in process control in LPBF, and identify the gaps in the state-of-the-art. Sec. 3 describes the experimental setup, build plan, exemplar parts studied, and methods for their characterization. Discussed in Sec. 4 is the development of model predictive process control approach, including a brief overview of thermal modeling using graph theory, and model validation. The results from applying DynamicPrint to three exemplar parts are reported in Sec. 5. Finally, summarized in Sec. 6 are conclusions and avenues for further research.

2 Literature Review of Process Control Approaches in LPBF

Process control, outlined in Figure 4, can be segmented into two broad approaches, namely, closed-loop, feedback control; and open-loop, feedforward control [35, 36]. The implementation of these approaches in the literature in the context of LPBF is discussed herewith. The DynamicPrint approach presented in this work falls in the category of feedforward control.

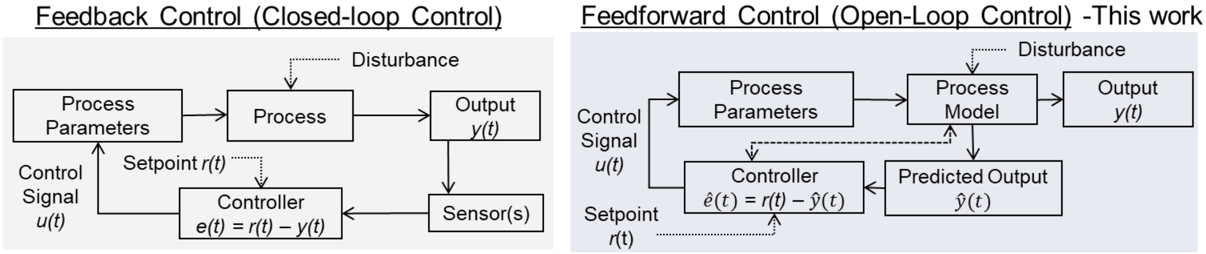

Figure 4: Comparison of closed-loop, feedback control and open-loop, feedforward control strategies. The DynamicPrint MPC approach presented in this work falls under the feedforward process control category.

2.1 Closed-Loop, Feedback Process Control

Referring to Figure 4, closed-loop control incorporates feedback from sensor(s) that measure the state of the process output $y(t)$, i.e., sensor(s) are connected to the output side of the process. Contingent on the data acquired from the sensors, the controller accesses the magnitude of a process drift $e(t) = r(t) - y(t)$, if any, from the desired setpoint $r(t)$ and produces a control signal $u(t)$ based on a mathematical model or heuristic algorithm to adjust the processing parameters designed to return the process to its nominal state. Thus, feedback control is reactive in nature as the control signal is generated after a process drift has been detected by sensors. Hence, there is an inherent lag before the process is returned to its nominal state [37].

Closed-loop, feedback control methods in LPBF use feedback from sensors, such as pyrometers, infrared thermal cameras, photodiodes, among others, to detect process drifts, and subsequently correct these by changing processing parameters [35, 38]. We note that there are currently no commercially available LPBF systems with an integrated feedback control mechanism [39]. An example of closed-loop control in LPBF was recently exemplified on a custom-built LPBF-setup by Wang *et. al.* [40]. They used photoresistors instrumented coaxially to the laser beam to observe the meltpool thermal emissions in the visible light spectrum. A feature called the thermal emission index was subsequently derived from the sensor data. The magnitude of the thermal emission index was used as the feedback signal to modulate the laser power via a proportional integral derivative controller. Wang *et al.* [40], demonstrated with single-layered parts made of Inconel 625 that control of the thermal emission resulted in a substantial mitigation in surface defects, including a reduction in overmelting, swelling and balling.

Renken *et. al.* [41] developed a closed-loop with LPBF control system using a pyrometer to detect the meltpool intensity. The controller compared the pyrometer signal to a predetermined set point and used proportional control to modify the laser power. When applied to a bridge-shaped part, the controller significantly reduced heat accumulation. A similar approach was applied by Adnan *et. al.* [42], who used two sensors, a coaxial and off-axis optical camera, to control and maintain a consistent meltpool emission in the LPBF process. The feedback controller was augmented by the off-axis optical camera, which assessed the surface quality through image analysis before and after the recoating process, and dynamically altered the targeted meltpool emission setpoint. The controller subsequently modulated the laser power and scan speed of cuboid geometries to improve subsequent layer quality.

Vasileska *et. al.* [43] used near infrared, co-axial imaging of the meltpool, specifically, meltpool shape and size as the control target. Process control was achieved through alteration of the duty cycle of a pulsed laser. This approach improved feature resolution of bridge-shaped parts, where reducing local heat accumulation prevented over-melting and geometric deviation. Instead of meltpool-based sensing, Kavas *et al.* [44] used an off-axis infrared thermal camera to acquire the interlayer part temperature. The interlayer temperature is stabilized layer-by-layer to avoid overheating. This is achieved by changing the laser power applied to the subsequent layer to maintain a constant inter-layer temperature. Kavas *et al.* [44] showed that the use of process control improved tensile strength in samples when compared to parts created without control of process parameters.

Recently, Malekipour *et al.* [45] proposed a theoretical framework for the control of LPBF by optimizing the scan sequence. The proposed strategy uses layerwise thermal tomography to identify localized heat accumulation caused by the previous layer scan strategy. This information is passed to thermophysical models similar to the graph theory thermal modeling approach used in this work. Information from the model is used to guide an optimization algorithm, which changes the subsequent layer scanning sequence. This adaptive scanning is hypothesized to reduce residual stress and part distortion. Recently, commercial LPBF systems with integrated feedback control mechanisms are being actively implemented [38, 39, 46]. For example, EOS recently introduced a closed-loop control system that dynamically adjusts the laser power to mitigate heat build-up, thus reducing need for of support structures [46].

2.2 Open-Loop, Feedforward Process Control (This work)

As outlined in Figure 4, open-loop or feedforward control does not incorporate feedback from the output state $y(t)$ of the process. Instead, disturbances are detected on the input side of the process. A physics-based or empirical model *predicts* the effect of the disturbance on the process output $\hat{y}(t)$. Based on the estimated drift, $\hat{e}(t) = r(t) - \hat{y}(t)$, from the setpoint $r(t)$ the controller and generates an appropriate control signal $u(t)$ to adjust the process parameters to avoid a potentially deleterious process drift before it occurs [36]. However, stochastic process drifts that affect the process output are not detected nor corrected in the feedforward, open-loop framework.

With this brief summary, we now describe the application of closed-loop and open-loop control to LPBF with the aid of select publications from the literature.

In the LPBF context, process adjustments in open-loop or feedforward control are made to the build plan before printing to compensate for a predicted process deviation. For example, the temperature distribution changes contingent on the cross-section, and certain features, such as overhangs, thin walls and internal channels tend to overheat. These predictions of the process deviation can be obtained using empirically derived or physics-based models, or a combination of the two approaches [22]. Based on insights from the model, the process parameters can be adjusted *a priori* to avoid deleterious thermal trends. The DynamicPrint approach in this work uses a physics-based thermal model to guide parameter adjustment before printing; it is a form of feedforward control.

An example of empirical model-based open-loop control was demonstrated by Yueng *et. al.* [47]. Their work developed a parameter termed geometric correction factor, which adjusts laser power *a priori* in response to the continually changing geometry. The geometric correction factor reduces the laser power when printing overhang regions. As a result, heat retention in the overhang was mitigated, which improved surface roughness. While the approach was computationally efficient, limited shapes were tested, and specific functional properties were not controlled.

An example of a model-based open-loop control in LPBF was demonstrated by Druzgalski *et. al.* [22]. They used the ALE3D FE simulation application developed by Lawrence Livermore National Laboratory [48]. Hatch-level thermal simulations were used as an input to a heuristic open-loop control strategy, which reduced heat accumulation in parts. This approach was demonstrated on a complex shape, which was tested with nominal parameters and the process parameters recommended by the feedforward control approach. The part produced with open-loop control showed improved surface and geometric integrity.

Wang *et. al.* [49] demonstrated the application of an open-loop control approach to limit formation of meltpool modes known to cause keyhole and lack-of-fusion porosity in LPBF. A FE-based model was developed to predict the change in thermal history of an LPBF geometry with two and five layers respectively. Controlling the laser power on a track level enabled a reduction of keyhole porosity formation. Ogoke *et. al.* [50] demonstrated the application of machine learning to open-loop control in LPBF. They used reinforcement learning to minimize defect formation occurrence in the LPBF process. The reinforcement learning algorithm attempted to maximize an empirically derived optimal meltpool distribution, and altered the process parameter conditions to maximize the time spent in this optimal meltpool condition. Recently, He *et al.* [31, 51] developed and applied a reduced order model for hatch-level simulation of the thermal history and resulting residual stresses. Their approach develops a custom scan strategy termed SmartScan that successfully reduces thermal-induced residual stresses and distortion in stainless steel 316L plate-like samples compared to default scan strategies.

In a recent work, Xi [52] compared the performance of closed-loop feedback control and feedforward MPC of meltpool width and depth. Xi's MPC approach is based on machine learning, and the feedback control mechanism is a proportional-integral-derivative algorithm. This theoretical study concluded that MPC is more effective than feedback control for attaining a desired meltpool depth and width. However, the foregoing study by Xi is concerned with meltpool-level control and does not involve building multi-layer parts [52]. By contrast, the model-predictive control approach in this work employs a physics-based model; is demonstrated on practical multi-layer parts; and assess the outcome of process control on functionally critical aspects of part quality.

This work differs from the aforementioned open-loop, feedforward control approaches in several ways. First, this work focuses on part-scale thermal control, as opposed to meltpool or hatch-level control, which is represented in a large body of existing research. Second, this work uses a form of iterative simulation to adjust the processing parameters on a layer-by-layer basis. This iterative simulation is possible due to the computational efficiency of the graph theory-based model [53]. The approach is demonstrated on both simple shaped parts and practical geometries. The control algorithm produced a process parameter plan within 5 hours for a complex bell crank part in this work. Lastly, we note that commercial LPBF machines change the laser power whilst scanning upskin and down-skin features encountered in overhang geometries. However, we underscore that the modified up-skin and down-skin process parameters are only applied to the contour regions; the process parameters are not altered between layers of the bulk section [54] . We note that upskin and downskin parameters suggested by the LPBF machine manufacturer (EOS) were also used in this work. Lastly, whilst build software, such as Materialise allow for determining build risks, such as possibility of a recoater crash, they do not provide a means to autonomously change the processing plan between layers based on a physics-based modeling to avoid these thermal-induced failures.

3 Methodology

3.1 Experiment Setup and Build Plan

In this work, ten stainless steel 316L (SS316L) parts were manufactured on an EOS M290 LPBF system. A schematic of the setup is shown in Figure 5. The LPBF machine is instrumented with a long wave infrared (LWIR) thermal camera to acquire the top surface temperature of each layer at a frame rate of 30 Hz. The data from the thermal camera is used for validation of the DynamicPrint approach. The camera was calibrated, as detailed in our previous works, to account for the effect of thermal emissivity [18]. The nominal processing parameters and other experimental conditions are listed in Table 1. The nominal process conditions for SS316L were suggested by the powder manufacturer based on prior experimentation. We note that these processing conditions include upskin and downskin adjustments suggested by the manufacturer.

The build plate with exemplar parts used in this work is shown in Figure 6. A total of 10 parts encompassing 5 different geometries were created. This paper focuses on results from 7 parts from three types of part geometries, labeled as the arch (A), trumpet (T), and bell crank (B). The parts range in height from 25 mm to 52 mm tall. The build required 12 hours to complete. Next, we describe each of the three geometries featured in this work. Thermal interaction between parts was mitigated by maintaining sufficient inter-part spacing, exceeding 10 mm where possible.

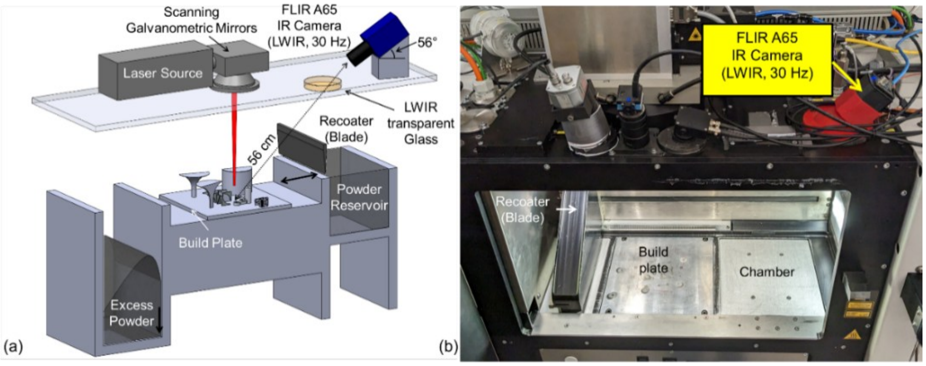

Figure 5: (a) Schematic of the EOS M290 system and the FLIR A65 long wave infrared (LWIR) camera installed in the system to capture thermal trends. The thermal camera is located outside

the build chamber and is focused on the build chamber via an infrared transparent window. (b) Picture of the experimental setup, with position of LWIR camera installed.

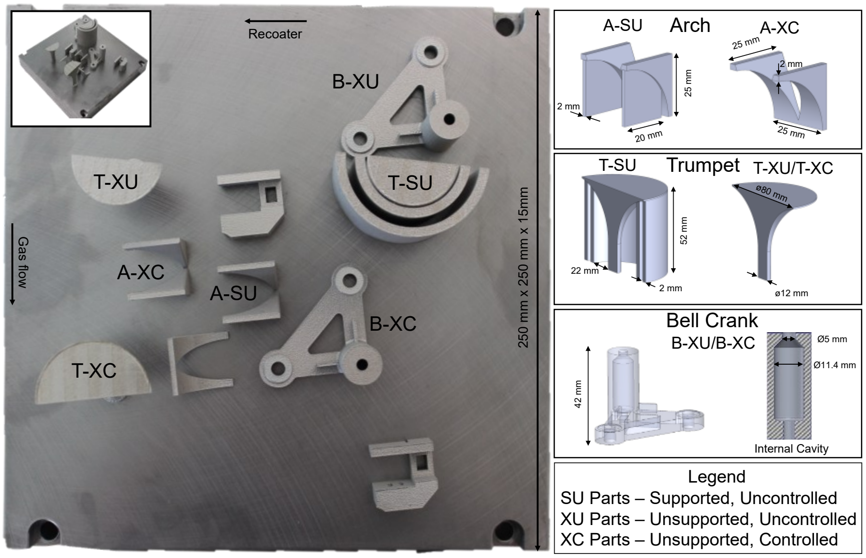

Figure 6: The finished build plate used to demonstrate the MPC approach of this work. Ten parts were created, with three unique geometries studied, with parts being termed the Arch (A), Trumpet (T), and Bell Crank (B). Parts were built with supports (S) and without support material (X), as well as, with (C) and without control (U). For example, the A-XC represents an arch-shaped part built without supports under controlled conditions.

Table 1: Processing conditions, materials properties, and sensor settings used in this work.

Nominal Processing Parameters [Units]	**Values**
Laser Power, P [W]	195
Scanning Velocity, V [mm·s^{-1}]	1083
Hatch Spacing, H [mm]	0.09
Layer Thickness, T [mm]	0.02
Volumetric Global Energy Density E_V [J/mm^3]	100
Build Conditions [Units]	**Values**
Build Atmosphere	Argon
Build Plate Preheat Temperature [°C]	70
Recoater Cycle Time or Powder Recoating Time [sec]	10
Recoater Blade Type	Metal
Powder Material Properties	**Values**
Material Type	Stainless Steel 316L
Material Manufacturer	Oerlikon
Powder Size Range [µm]	15 – 45 (D10 – D90)
IR Thermal Camera Specifications	**Values**
Brand and Model	FLIR A65
Resolution [pixels], [pixel per mm^2]	640 × 512, 103
Frame Rate [Hz]	30
Spectral Range [µm]	7.5 to 13
Temperature Range [°C]	40 to 550
Camera On Trigger Event	Continuous

3.2 Exemplar Part Geometries

Referring to Figure 6, three types of part geometries are studied in this work, namely, arch (A), trumpet (T), and bell crank (B). Two more aspects define each of these part geometries. First, parts were either built with supports structures (S) or without supports (X). Second, parts were either built under nominal processing conditions that remain fixed for all layers, termed uncontrolled processing (U) or with layer-by-layer DynamicPrint (C). For example, A-XC represents an arch-shaped part without supports processed using DynamicPrint. We herewith describe each of these geometries, and their rationale.

3.2.1 Arch

Two 25 mm tall arch-shaped parts consisting of 1250 layers were built; these are labeled as follows.

(i) Supported, uncontrolled arch (A-SU) built under uncontrolled conditions with laser power fixed at 195 W and solid support material added underneath the overhang. The arch part with supports embodies the ideal thermal history ($\widehat{\mathrm{T}}_{\mathrm{ideal}}$).

(ii) Unsupported, controlled arch (A-XC) built without support structures and with layer-by-layer laser power changes recommended by the model-predictive control strategy.

The justification of selecting the thermal history of the supported, uncontrolled arch (A-SU) as the ideal or target thermal history ($\widehat{\mathrm{T}}_{\mathrm{ideal}}$) is tendered herewith. In our previous work, it was demonstrated that arch-shaped parts with unsupported spans, despite being manufactured under optimized processing conditions, caused recoater crashes due to heat accumulation in the overhang region [2]. By contrast identical arch-shaped parts with supports avoided recoater crashes [2]. This is because, supports provided a thermal pathway to conduct heat away from the overhang region thus avoiding recoater crashes [55]. Consequently, parts with supports tend to depict a more even thermal history, which is favorable to several aspects of part quality ranging from surface finish, residual stresses to microstructure [55]. Hence, it is customary to build support structures when printing large overhang spans.

A typical design guideline is to support arch-shaped parts with greater than 0.5 mm horizontal overhang [56]. However, the supports increase processing time, material, and removal of supports requires substantial post-process machining and finishing. It is estimated that post-process support removal accounts for as much as 50% of the total cost of an LPBF part [57]. Therefore, it would be economically valuable to eliminate supports in arch-shaped parts while avoid build risk, and retaining the beneficial aspects of a homogenous thermal history. Consequently, we printed an arch-shaped part without supports (A-XC) having the same thermal history as a arch-shaped part with support (A-SU).

The DynamicPrint approach is adapted in the following manner to avoid recoater crashes and eliminate support structures in the arch-shaped parts. The laser power, while processing the arch-shaped part without supports (A-XC), is adjusted layer-by-layer such that its thermal history matches the thermal history of the arch-shaped part built with supports (A-SU, $\widehat{\mathrm{T}}_{\mathrm{ideal}}$). Although for comparison purposes it would be desirable to build an arch-shaped part (A-XU) without supports under constant (uncontrolled) laser power conditions of 195 W, this is not attempted herein as it is highly susceptible to initiate a recoater crash, and as a consequence, jeopardize the entire build and damage the recoater blade [2, 58].

3.2.2 Trumpet

Three trumpet-shaped geometries each 52 mm tall (2600 layers) were built as follows.

(i) Unsupported, uncontrolled trumpet (T-XU) built under uncontrolled processing conditions, with laser power fixed at 195 W, and without supporting material.

(ii) Supported, uncontrolled trumpet (T-SU) built under uncontrolled processing conditions with laser power fixed at 195 W, and with supporting material. The layer-wise average thermal history of T-SU is the ideal thermal history ($\widehat{\mathrm{T}}_{\mathrm{ideal}}$) that the controller strives to achieve.

(iii) Unsupported, controlled trumpet (T-XC) built without supporting material, but with laser power controlled layer-by-layer. As with the arch-shaped parts, the rationale is to eliminate supports by ensuring that the thermal history of the unsupported trumpet part (T-XC) matches that of the supported trumpet (T-SU, $\widehat{\mathrm{T}}_{\mathrm{ideal}}$).

These trumpet shaped parts have an overhang angle that increases progressively with the deposited layers. While the overhang of the trumpet is more gradual than the arch-shaped part, the part itself is substantially taller. As a result, heat retention is likely to be exacerbated in later layers, potentially causing a recoater crash. Further, the grain coarsening increases proportionally with heat retention, while the variation in microhardness also increases [19]. Consequently, an increase in terms of the primary dendritic arm spacing, and variation in microhardness is expected in the unsupported, uncontrolled trumpet (T-XU) [19]. The supports structures in T-SU prevent heat retention, and mitigate subsequent grain coarsening and variation in microhardness by providing a thermal pathway to conduct excess heat from the overhang to the substrate.

3.2.3 Bell crank

Two 42 mm tall bell crank parts consisting of 2100 layers were built as follows.

(i) Unsupported, uncontrolled (B-XU) with laser power fixed at 195 W.
(ii) Unsupported, controlled (B-XC) with laser power modulated layer-by-layer.

Support structures were not required for the bell crank, as it is oriented with the shaft facing upwards. The bell crank is use-inspired, it is a critical linkage mechanism in aircraft and automotive controls. The bell crank shape particular to this work has a 42 mm tall shaft with a cavity that has varying diameter and an internal overhang feature. The cavity with overhang, is difficult, if not impossible, to access using standard subtractive machining tool. Consequently, the as-built surface roughness of the cavity is critical to functional properties, such as fatigue life.

It was noted, based on X-ray CT imaging, that the internal surface of the as-built cavity for the uncontrolled bell crank (B-XU) had relatively poor surface integrity likely due to heat accumulation within the shaft. Heat accumulation led to partial melting of surrounding particles, degrading surface integrity. Therefore, it was hypothesized that the surface integrity, particularly of internal features, would be improved by minimizing the heat accumulation within the shaft. Accordingly, the aim of the DynamicPrint is to adjust the laser power, such that thermal history of the bell crank (B-XC) has a constant temperature trend. Hence, for the bell crank part, the ideal thermal history ($\widehat{T}_{ideal}$) is determined to have a constant average layer temperature of 75 ºC.

3.3 Build Parameter Selection

The parameters for the current work were selected based on a recently published work with the identical material (SS 316L) and on the same machine (EOS M290) [59]. In this previous work, we manufactured 40 tensile ASTM E8 tensile (dogbone) samples under various power (P), velocity (V), hatch spacing (H) conditions. We further studied the effect of processing conditions on porosity formation and mechanical properties. Materials characterization included optical microscopy (OM), scanning electron microscopy (SEM), electron backscatter diffraction (EBSD), X-ray diffraction (XRD), X-ray CT (14 μm voxel resolution), and microhardness. This was followed by tensile strength and yield strength measurement with digital image correlation (DIC), followed by fractography analysis.

In the foregoing published work, the nominal energy density $E_v = 100$ J·mm^{-3}, with P = 195 W, V = 1100 mm·sec^{-1}, T = 0.020 mm [59]. At this nominal processing condition there was no evidence of keyhole porosity or lack-of-fusion porosity formation observed in the tensile samples via X-ray CT optical microscopy and SEM. The nominal conditions in the current work are almost identical: P = 195 W, V = 1083 mm·sec^{-1}, H = 0.090, and T = 0.020 mm resulting in $E_v \sim 100$ J·mm^{-3}.. Likewise, porosity was not detected in the current parts through SEM imaging and X-ray CT.

In the prior work, the highest energy density $E_v = 125$ J·mm^{-3} with P = 225 W, V = 1000 mm·sec^{-1}, H = 0.090 mm, and T = 0.020 mm. Despite this high energy density, keyhole porosity was not observed in the tensile samples either through optical microscopy and SEM. Therefore, to diminish the chance of keyhole porosity in the current work, the energy density is restricted to $E_v = 115$ J·mm^{-3} by slightly increasing the scan velocity, accordingly the highest allowable laser power in this work is P = 225 W, with V = 1083 mm·sec^{-1}, H = 0.090, and T = 0.020 mm.

For manufacturing the tensile specimens, the lowest energy density was $E_v \sim 73$ J·mm^{-3} which did not show any incidence of lack-of-fusion porosity either through optical microscopy, SEM, and X-ray CT. Therefore, to precluded lack-of-fusion porosity in the current work the lowest energy density was maintained at $E_v = 74$ J·mm^{-3} with minimum laser power reduced to P = 145 W. Lack-of-fusion porosity was not observed in any of the current parts either X-ray CT (voxel resolution 16 μm) or SEM. Thus, adjusting the laser power between the set laser power range of 146 W and 225 W did not adversely affect the density of the parts.

The density of the parts in this work can be estimated based on our prior work [59]. The tensile samples post-processed with electro-discharge machining and examined with SEM and X-ray CT at voxel resolution of 14 μm. The samples devoid of visually apparent porosity in the X-ray CT slices and SEM images had a defect volume ratio (DVR) ranging between 0.001% to 0.004%.

Microhardness, and tensile and yield strength measurements were conducted on the ASTM E8 specimens using DIC [59]. For test specimens with porosity, the corresponding mean Vickers microhardness readings were less-than 210 HV, and the tensile strength was ~ 620 MPa (yield strength ~ 510 MPa). By contrast, for the test samples devoid of porosity, the microhardness was ~224 HV, with the corresponding tensile strength ~650 MPa (yield strength ~ 580 MPa). In the current work, whilst it is not possible to conduct mechanical tests due to the complex shape of the parts, however, for all samples, either controlled or uncontrolled, the mean microhardness exceeded 224 HV. This further affirms that the samples in this work were not affected by porosity.

3.4 Post-Process Characterization

3.4.1 X-ray CT to ascertain absence of lack-of-fusion porosity, surface and geometric integrity.

After processing, the parts were examined with X-ray computed tomography (X-ray CT) on a North Star Imaging X3000 system with ~16 µm voxel resolution to ascertain lack-of-fusion porosity, and surface and geometric integrity of internal features. This X-ray CT resolution is insufficient for determination of microstructure related aspects beyond lack-of-fusion porosity, such as grain size and keyhole porosity. None of the samples in this work showed presence of lack-of-fusion porosity – a result affirmed through SEM.

We note that to examine the SS 316L samples in this work, whose maximum dimensions are greater than 10 mm, the X-ray CT machine had to be set at its maximum voltage 225 kV. The best possible voxel resolution at this scan voltage was 16 µm. While, increasing the X-ray CT beam voltage would allow examination of larger sample thickness, but doing so would also increase the X-ray beam spot size, and therefore degrade the voxel resolution. In other words, there is a tradeoff between beam voltage, voxel resolution and sample thickness.

3.4.2 Scanning electron microscopy (SEM) to measure primary dendritic arm spacing (PDAS, λ_1) and confirm absence of lack-of-fusion and keyhole porosity porosity.

The primary dendritic arm spacing (PDAS, λ_1) has a significant effect on mechanical properties, such as microhardness and strength. Smaller grain sizes and PDAS correlate with larger microhardness, enhanced part strength and creep [60, 61]. To measure PDAS, samples of the trumpet and arch parts were polished and etched with aqua regia (3 HCl:1 HNO_3) and were examined using SEM at 6000× magnification with a beam accelerating voltage of 10 kV.

Multiple locations per part were analyzed with three representative images taken at each location. The SEM images are approximately 30 µm × 20 µm. For example, as many as 9 locations were scanned for the trumpet-shaped part. The PDAS measurements from these images were acquired using the recommended bounding box procedure detailed in our previous works [19]. As affirmed in our previous work, using X-ray diffraction (XRD) analysis, the material stainless steel 316L is a single-phase austenitic grade steel, hence XRD analysis was not conducted in this work [59]. The SEM images confirmed that the samples were devoid of both lack-of-fusion and keyhole porosity.

Further, to affirm the absence of keyhole and lack-of-fusion porosity, wide field-of-view (~625 μm × 450 μm) SEM images were also acquired at 200× magnification. These SEM micrographs visualize nearly 25 layers of deposited material. None of the SEM images for any of the parts showed presence of either keyhole or lack-of-fusion porosity.

3.4.3 Microhardness

The complex geometries manufactured in this work are not amenable for mechanical testing. In this work, we have conducted microhardness readings, as a surrogate for mechanical testing. The Vickers microhardness of the trumpet-shaped parts was determined using a LECO LM110 microhardness tester. The microhardness was measured at 300 gm load for a dwell time of 10 seconds ($HV_{0.3, 10}$).

4 DynamicPrint Model Predictive Control

4.1 Control Algorithm

The DynamicPrint approach is an embodiment of model predictive control (MPC). The conceptual basis of MPC, as applied to LPBF in this work, is to iteratively adjust the laser power over a finite future time horizon (layers) subject to constraints [26, 62]. The four steps in the MPC approach are: Predict, Identify, Parse, and Select. These steps are summarized in Figure 7, with a temporal schematic diagram of the control algorithm in the context of the arch-shaped part.

Step 1 Predict

Given a part geometry along with its material properties, time between layers, and nominal processing parameters, we use a rapid, meshless physics-based simulation model to predict its thermal history [25]. In this work, the thermal history is predicted for the part geometry under fixed processing conditions ($P = 195$ W, $V = 1083$ mm·s^{-1}, $H = 90$ µm, $T = 20$ µm).

These thermal simulations required less than 15 minutes to complete for each geometry. This so-called uncontrolled, or original thermal history, is denoted as $\widehat{\mathrm{T}}_{\mathrm{original}}$ in the red dotted line of Figure *7*. We note that the uncontrolled and unsupported arch-shaped part (A-XU) is liable to overheat as evident from the steep rise in layer-wise average end-of-cycle layer temperature.

Step 2 Identify

Next, we identify the ideal or target ($\widehat{\mathrm{T}}_{\mathrm{ideal}}$) thermal history to preclude the identified deleterious thermal trends in $\widehat{\mathrm{T}}_{\mathrm{original}}$ from Step 1. The ideal thermal history can either be determined from another instance of a similar geometry with desirable thermal trends, or heuristically by the operator. In this work the use of both strategies were demonstrated, the former for the arch and trumpet geometries, and the latter for the bell crank.

For example, as shown in our previous work, the arch-shaped part when manufactured without support material and constant laser power often fails to build due recoater contact [2]. Hence, to avoid heat retention, practitioners design support structures to conduct the heat away from the overhang regions to the substrate [55, 63]. However, as explained before, support structures increase the build time and amount of material required, and necessitate considerable post-process machining to remove, thus increasing the cost of the part [57]. Therefore, it would be valuable to the practitioner to minimize, if not eliminate, support structures [64].

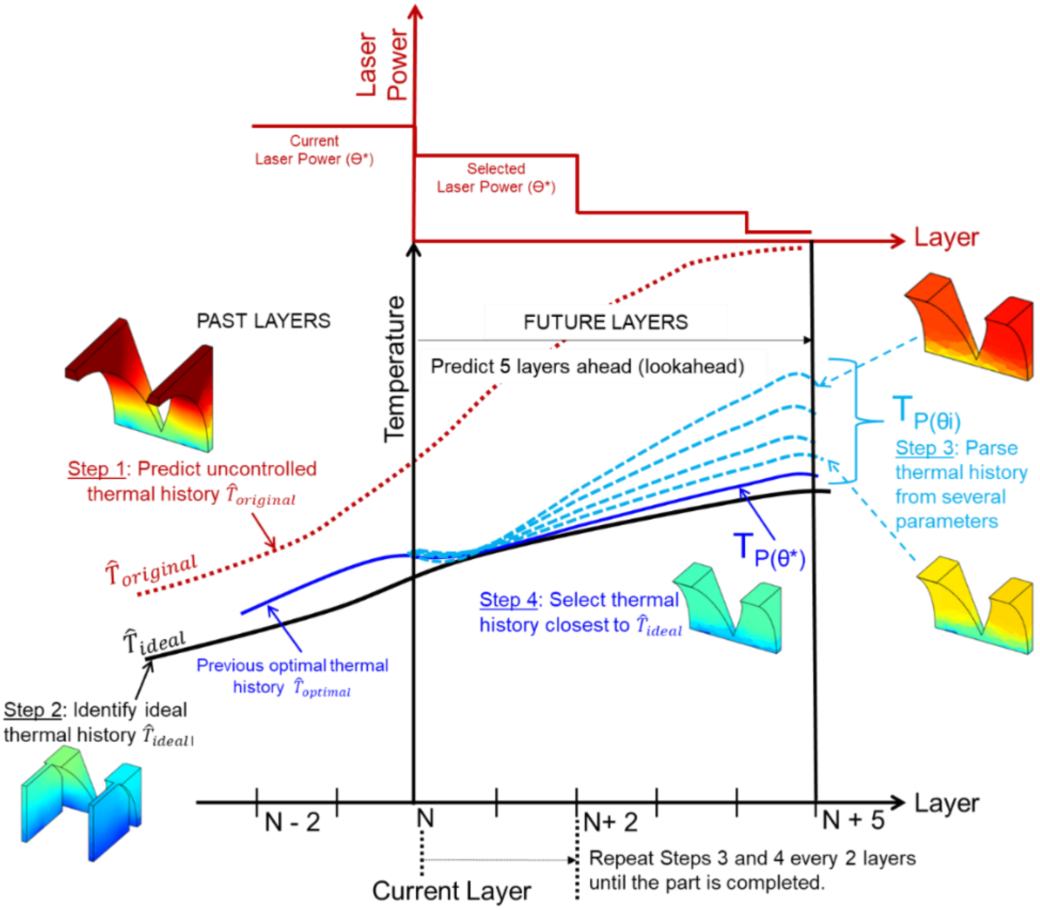

Figure 7: Graphical summary of the DynamicPrint MPC method and its temporal behavior. The process is completed in four steps, (1): Predict the uncontrolled thermal history. (2): Identify ideal thermal history. (3): Parse thermal history from multiple process parameters simultaneously for five future layers. (4): Select ideal thermal history and process parameters. Steps (3) and (4) are repeated every two layers to generate the final process parameter recommendations.

Accordingly, $\widehat{\mathrm{T}}_{\mathrm{ideal}}$ was chosen as the target thermal history of an arch-shaped part built with anchoring supports (A-SU). The $\widehat{\mathrm{T}}_{\mathrm{ideal}}$, shown as a thick black line in Figure 7, is also obtained using the graph theory model This strategy was also utilized for the trumpet-shaped part. In other words, the target thermal history ($\widehat{\mathrm{T}}_{\mathrm{ideal}}$) for the arch (A-XC) and trumpet-shaped (T-XC) parts without supports are the dynamic thermal history of the corresponding parts with supports, A-SU and T-SU, respectively. By contrast, a constant end-of-cycle temperature of 75 ºC was set as the target $\widehat{\mathrm{T}}_{\mathrm{ideal}}$ for the bell crank geometry. Essentially, the thermal history or the bell crank was chosen to have a ceiling value to reduce heat accumulation and avoid uneven temperature distribution, which was shown in our previous work to result in increased surface roughness, geometric inaccuracy, and microstructure heterogeneity [18].

Step 3 Parse

At every simulation epoch, the thermal history of the part is predicted as a function of various laser power levels, within constraints, layer-by-layer over a fixed spatiotemporal horizon of future layers. To explain further, consider layer N of the part, the thermal history $\widehat{\mathrm{T}}_{\mathrm{P}(\theta_i)}$ is predicted as a function of *h* candidate laser power settings $\mathrm{P}(\theta_i)$ for k future layers, *i* = $\{1 \ldots h\}$. Thus, from the graph theory model, the end-of-cycle temperatures for layers N through N+k are determined for laser power levels $\mathrm{P}(\theta_i)$, i.e., $\widehat{\mathrm{T}}_{\mathrm{P}(\theta_\mathrm{i})}(\mathrm{N}+0), \widehat{\mathrm{T}}_{\mathrm{P}(\theta_\mathrm{i})}(\mathrm{N}+1) \ldots \widehat{\mathrm{T}}_{\mathrm{P}(\theta_\mathrm{i})}(\mathrm{N}+\mathrm{k})$. In this work, the prediction horizon k = 5 is called *lookahead*, and the number of candidate laser power settings, *h* = 5. Five discrete levels of laser power were analyzed: θ_1 = 146 W, θ_2 =156 W, θ_3 = 176 W, θ_4 = 195 W, and θ_5 = 225 W. Noting that θ_4 = 195 W is the nominal laser power.

The laser power is constrained between 146 W and 225 W, so as to avoid lack-of-fusion porosity beyond the lower limit, and keyhole porosity at the upper limit based on results reported in the literature for SS316L [65]. Discrete power levels are chosen to mitigate the computational burden and facilitate practical application, as the power levels adjustments are manually entered into the LPBF machine by the operator before printing. We note that the graph theory thermal simulation implements a meta-layer approach where multiple layers are considered to be deposited at once. This simplification is also inherent to most FE-based commercial software [66]. Here, 5 actual layers (100 μm) correspond to 1 simulation layer. Hence, the simulation lookahead of k = 5 corresponds to 500 μm of actual build height.

Step 4 Select

After the layer-wise thermal history $\widehat{T}_{P(\theta_i)}$, i = {1...5} from each of the five laser power levels are simulated, we select the optimal laser power θ^* which results in the minimum mean absolute deviation (MAD) from the ideal thermal history $\widehat{T}_{\mathrm{ideal}}$ over the next five layers. Mathematically, the control strategy is expressed as follows.

$$\theta^* = \underset{\substack{\theta \\ \theta=\{\theta_1\ldots\theta_5\}}}{\arg\min} \sum_{k=0}^{k=5} \frac{\left|\widehat{T}_{\mathrm{ideal}}(N+k) - \widehat{T}_{P(\theta)}(N+k)\right|}{k} \tag{1}$$

Thus, the optimal thermal history for layer N is $\widehat{T}_{\mathrm{optimal}}(N) = \widehat{T}_{P(\theta^*)}$.

The rationale for selecting the minimum mean absolute deviation is that it suppresses both positive and negative deviations from the target thermal history ($\widehat{T}_{ideal}$). If the minimum were to be selected as the objective function, it would only mitigate positive excursion from the target.

Steps 3 and 4 are repeated after every two simulated layers, i.e., N is replaced by N + 2 in the next step. Hence, the optimal laser power is determined in 200 μm intervals for the entire part [65]. In other words, the thermal history of the controlled geometry is optimized for 5 future layers (500 μm), and recalculated (rollback) every 2 layers (100 μm). The model control scheme was able to complete and identify the optimal laser power θ^* for all layers in approximately five hours for the bell crank geometry. For ease of practical implementation, two further simplifications are made to the laser powers recommended by the controller.

i. In our previous work, we observed defects at the interface of layers where large process parameter changes occur [67]. Therefore, to reduce the severity of the process parameter changes a 15-point moving average is applied to the laser power plan generated by the controller. This 15-point moving average corresponds to 1.5 mm of build height.
ii. Since the layer-wise adjusted laser power settings θ^* must be manually entered into the LPBF machine by the operators. To aid implementation, the smoothened laser power recommendations were further averaged for every 4 mm window of build height (200 layers). Simulation studies showed minimal differences between the end-of-cycle temperature for the as-predicted and smoothed laser power estimates.

4.2 Thermal History Prediction with Graph Theory

DynamicPrint relies on rapid and accurate prediction of the thermal history $\widehat{\mathrm{T}}_{\mathrm{P}(\theta_i)}$ as a function of laser power level i, iteratively every 2 layers, in Step 3. Thermal modeling using FE-based methods are ill-suited for implementation of the iterative steps in DynamicPrint owing to their computationally intensive nature [68, 69]. The mesh-free graph theory thermal modeling approach overcomes this drawback [18, 25].

We now provide a brief overview of the graph theory approach used in this work. Detailed mathematical treatment, including verification with FE analysis, exact analytical Green's functions solutions, and validation with experiments of the approach is available in our prior publications [25, 53, 70, 71]. As with the FE-based approaches, the graph theory model solves the heat diffusion equation to obtain the temperature for each point T(*x,y,z*) at every sampled point in time (*t*). This relationship is defined in Eqn. (2).

$$\rho c_p \frac{\partial \mathrm{T}(x,y,z,t)}{\partial t} - k\overbrace{\left(\frac{\partial^2}{\partial x^2}+\frac{\partial^2}{\partial y^2}+\frac{\partial^2}{\partial z^2}\right)}^{Laplacian\ operator}\mathrm{T}(x,y,z,t) \; = \mathrm{Q} \qquad (2)$$

In Eqn. (2), ρ is the material density [kg·m^{-3}], c_p is the specific heat [J·kg^{-1} ·K^{-1}], k is the conductivity [J·s^{-1} ·m^{-1}·K^{-1}], and Q is the rate of heat supplied per unit volume of material melted [J·s^{-1}·m^{-3}], called volumetric heat flux. Material properties are assumed to be fixed and are evaluated at 250°C. The term $\mathrm{Q} = \frac{\mathrm{A_e P}}{\mathrm{V \cdot H \cdot L} \cdot t}\ [\frac{\mathrm{W}}{\mathrm{mm^3}}]$ is a function of the processing parameters: laser power (P, [W]), laser velocity (V, [m·s^{-1}]), hatch spacing (H, [m]), layer height (L, [m]), and time when the laser is active (*t*, [s]). The term $\mathrm{A_e}$ in Eqn. (2) is the effective laser absorptivity.

The graph theory thermal model replaces the second derivative continuous Laplacian operator $\left(\frac{\partial^2}{\partial x^2}+\frac{\partial^2}{\partial y^2}+\frac{\partial^2}{\partial z^2}\right)$ in Eqn. (2), with a spatial discrete Laplacian matrix (L). This term represents the shape of the part. The thermal history $\mathrm{T}(x,y,z,\mathrm{t})$ is obtained as a function of the eigenvalues (Λ), eigenvectors (ϕ) of the Laplacian matrix (L) after simplification [25].

$$\mathrm{T}(x,y,z,\mathrm{t}) = \overbrace{\phi e^{-\frac{k}{\rho c_p}\Lambda t g}\phi'}^{Part\ Shape\ and\ time}\ \overbrace{\left(\frac{\mathrm{A_e S_l}}{\rho v c_p}\frac{\mathrm{P}}{\mathrm{V}} + \widehat{\mathrm{T}}_{\mathrm{prev}}\right)}^{\substack{Processing\\ Conditions}} \qquad (3)$$

In this work, A$_e$ = 0.60 based on experiments by Ye *et al.* at Lawrence Livermore National Laboratory [72]. Next, $\mathrm{S_l}$ is the length scanned per layer (a function of hatch spacing, [mm]), P [W] laser power, V [mm·s^{-1}] laser velocity, v [mm^3] volume of material melted in a layer (a product of scanned area and layer height), $\widehat{\mathrm{T}}_{\mathrm{prev}}$ [°C] is the temperature of the previous layer (from simulation), g = 0.6 the unitless gain factor is included in the exponent term to adjust the cooling rate, and *t* is the time required for processing the current layer. The dissipation of heat via the conduction equation in graph theory is followed by losses at the boundary of the part through convection and radiation.

An important quantity in Eqn. (3) is the time *t*, termed inter-layer time (ILT), often also called time between layers. The ILT is not constant, but changes proportionally to the top surface area of all parts in each layer. The ILT evolution for this work is shown in Figure 8. During the start of the build the ILT is nearly 70 s, and reduces to 40 s near layer 2000, as most of the parts have finished printing. The ILT was estimated a priori based on the cross-section area, hatch spacing, laser velocity. The ILT includes the time to recoat a fresh layer of powder. The powder recoat time was measured to be constant of 10 seconds as noted in Table 1. A low ILT increases the bulk part temperature, conversely, increasing the ILT reduces heat retention [18].

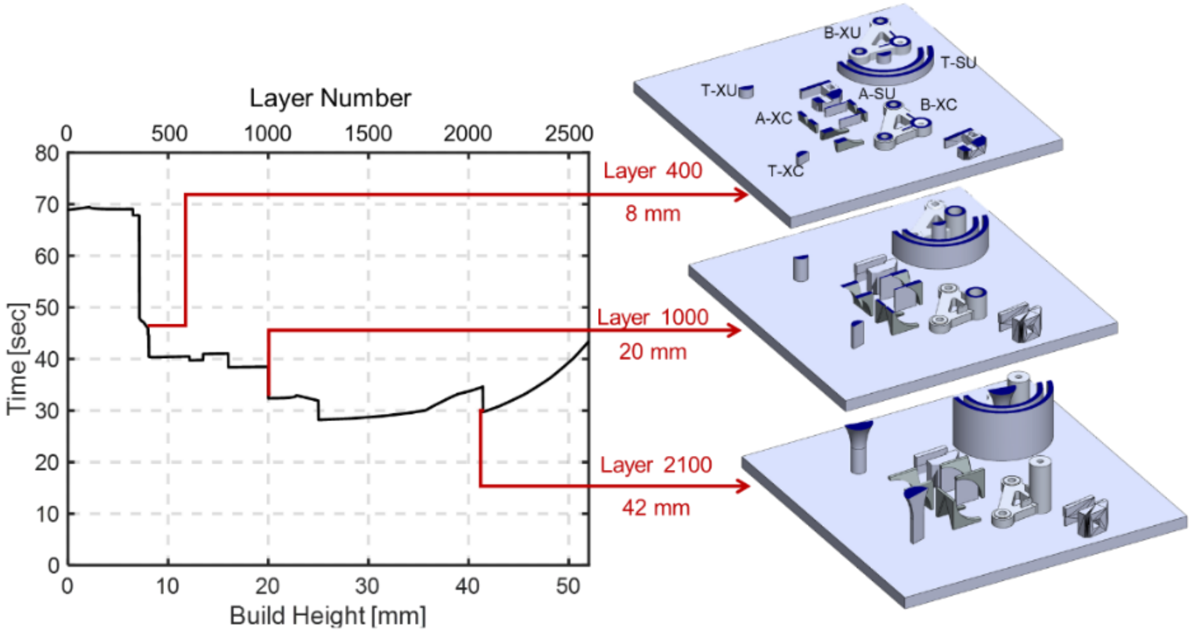

Figure 8: Inter-layer time (ILT) plotted as a function of build height. Because parts completed at different build heights, the ILT steadily reduced throughout the build. Shorter ILT values result in increased heat accumulation due to a reduction in cooling time for each deposited layer.

4.3 Salient Aspects of the Graph Theory Thermal Modeling Approach

A salient aspect of the graph theory thermal solution in Eqn. (3), is that the part shape and cooling time are decoupled from the processing conditions, such as laser power (P) and velocity (V). Consequently, for a given part shape, the eigenvalues (Λ), eigenvectors (ϕ) of the Laplacian (L) can be pre-calculated for each part layer, and the effect of multiple different process parameter settings can be ascertained without significant computational overhead, and without having to re-mesh the part as in FE analysis [68, 69]. The semi-analytical nature of Eqn. (3), i.e., discrete in space and continuous in time, allows rapid prediction of thermal history as a function of various laser power levels in an iterative manner. For example, each parameter iteration of the trumpet-shaped part in step 3 was completed within 5 minutes, and the optimal parameters were identified autonomously within 6 hours. Further, the semi-analytical nature of the solution also eliminates the need for stepping through time, further reducing the computational burden.

To reduce the computational time, researchers are actively developing alternatives to FE-based modeling, such as finite difference and thermal circuit networks [73, 74]. In our recent works, we have benchmarked FE, analytical modeling (Greens' functions), finite difference, and graph theory solutions for solving standard heat transfer and additive manufacturing cases [25, 70]. In these prior works, the aforementioned models were implemented with identical, temperature invariant materials properties. Indeed, we have compared the graph theory solution with FE for a large LPBF part whilst maintaining temperature invariant material properties [71]. The foregoing studies showed that the rapid convergence of graph theory was not on account of ignoring variable material properties.

The main reasons for the rapid convergence of the graph theory model approach are two-fold: (i) In FE-based approaches the part has to be repeatedly re-meshed with the addition of material.

This re-meshing step is computationally cumbersome. (ii) The graph theory approach is semi-analytical in nature, and the effect of part shape and cooling time are decoupled from the processing conditions, as described in the context of Eqn. (3) above. As a consequence, the effect of processing parameters on thermal history can be rapidly iterated without having to compute the solution to the heat equation.

4.4 Model Calibration and Validation

All thermal simulations require boundary conditions to capture the effects of the machine, build plate and gas flow on thermal history [69]. Heat losses are computed by augmenting the Laplacian matrix (L) with Type 3 (convection) boundaries [19, 25]. Model calibration involves experimentally determining the following three heat transfer boundary coefficients: bulk heat loss assigned to the build plate (h_s); convective heat loss to the surrounding powder (h_p); and, forced convection heat loss from the top surface (h_g). These heat transfer boundary coefficients were calibrated on the same machine and material by means of a separate build conducted *a priori*. The method for tuning the heat transfer boundary coefficients in the graph theory thermal model is detailed in our previous works [2, 18]. The calibration process is identical to the model validation approach described below. The calibrated heat transfer coefficients are reported in Table 2.

The graph theory thermal model was calibrated and validated using data from the longwave infrared (LWIR) thermal camera. The LWIR camera itself was calibrated using industry-standard methods discussed in our previous works [2]. The IR camera acquires thermal images of the top surface at 30 Hz. From this data, end-of-cycle top surface temperature measurements were extracted according to the method summarized in Figure 9. Shown in Figure 9(a) is a calibrated IR image obtained from the thermal camera. The IR measurements acquired over six layers for a specific region of interest of the trumpet part is shown in Figure 9(b). The plotted region of interest is 1 mm x 1 mm. The sharp peaks in Figure 9(b) result from the laser passing over the sample region in the current layer.

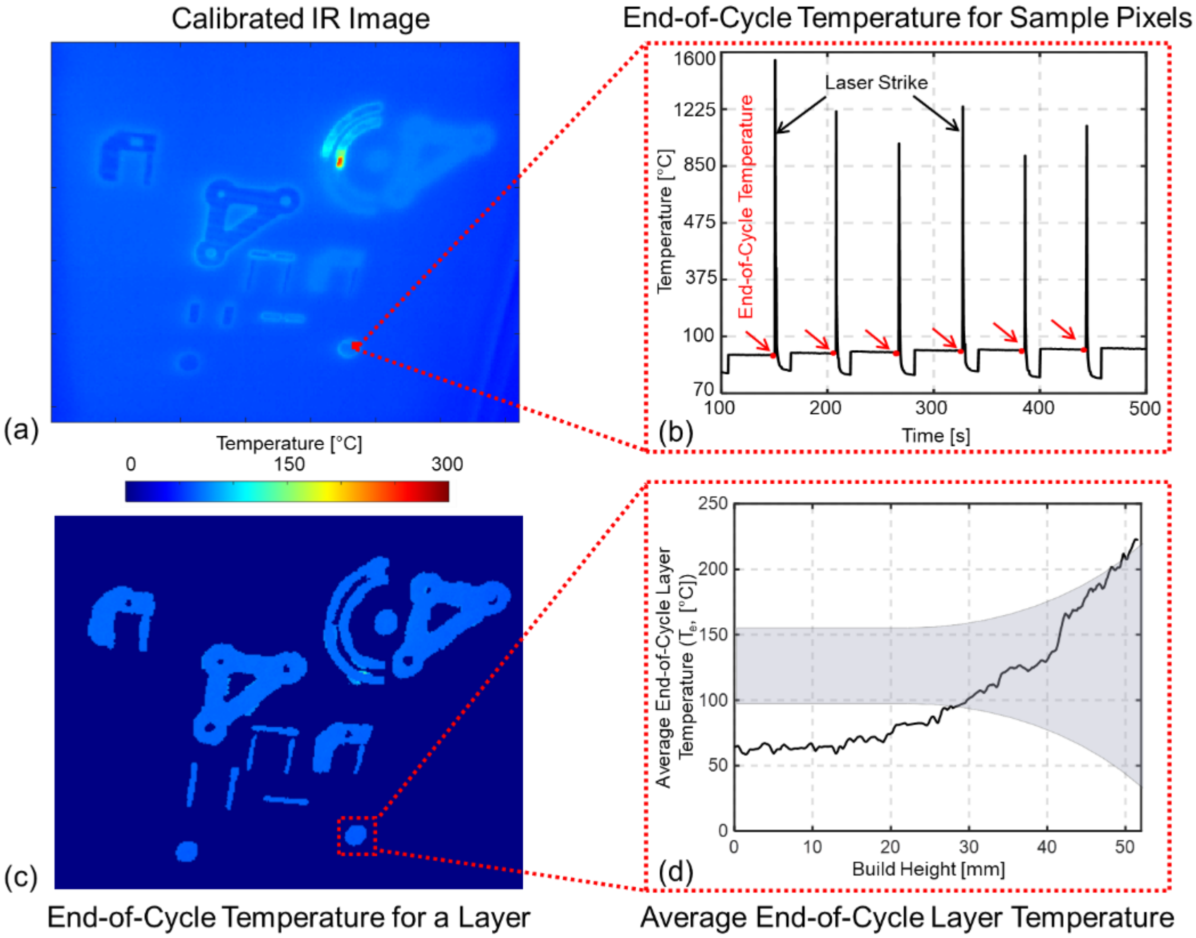

Figure 9: The procedure to extract the end-of-cycle surface temperature (T_e) from the infrared thermal images. (a) Calibrated top surface temperature images from the IR camera. (b) Temperature measurements for a single 1mm × 1mm region over six layers. The end-of-cycle temperature is measured at the moment just before the laser strike. (c) The end-of-cycle temperature was calculated for all pixels, resulting in the end-of-cycle composite image for an entire layer. (d) The average end-of-cycle layer temperature (T_e) was obtained by averaging the temperature of the part over the layer.

The end-of-cycle surface temperature is extracted from this time-based data by measuring the temperature immediately before the laser passes the selected region of interest as demonstrated in Figure 9(b). The end-of-cycle temperature of all parts in a layer is shown in Figure 9(c). Reported in Figure 9(d) is the end-of-cycle temperature averaged over each layer of the unsupported, uncontrolled trumpet-shaped part built under fixed laser power (T-XU). This steady-state layer averaged end-of-cycle layer temperature is termed T_e and was used as the metric for process control. The end-of-cycle layer temperature is analogous to the inter-pass temperature in the welding literature, it is also called residual surface temperature [75].

Shown in Figure 10 is the composite image of end-of-cycle top surface temperature for various parts on the build plate for select layers. A limitation with T_e as a control metric is that it occludes temperature differences between different regions of the part within the same layer; i.e., local temperature variations are suppressed. However, for the exemplar parts printed in this work the bulk section of the part is sufficiently large to negate local temperature variations. Further, T_e for a layer is influenced by preceding layers. This effect is captured in Eqn. (3) in terms of $\widehat{T}_{\text{prev}}$, viz., the predicted temperature of the previous layer.

The average end-of-cycle layer temperature (T_e) measured from the thermal camera is compared to its counterpart $\widehat{T}_e$ predicted by the graph theory thermal model in Figure 11. The graph theory model predictions ($\widehat{T}_e$) are between 2.5% to 8% symmetric mean absolute percentage error (SMAPE) of the observed end-of-cycle layer temperature (T_e). In temperature units the prediction error is between 5°C and 20°C (root mean squared error, RMSE). The bell crank geometry (B-XU) required the longest time to converge at 15 minutes. The arch (A-SU) and trumpet (T-XU) geometries required approximately 11 and 10 minutes, respectively. The model parameters are reported in Table 2.

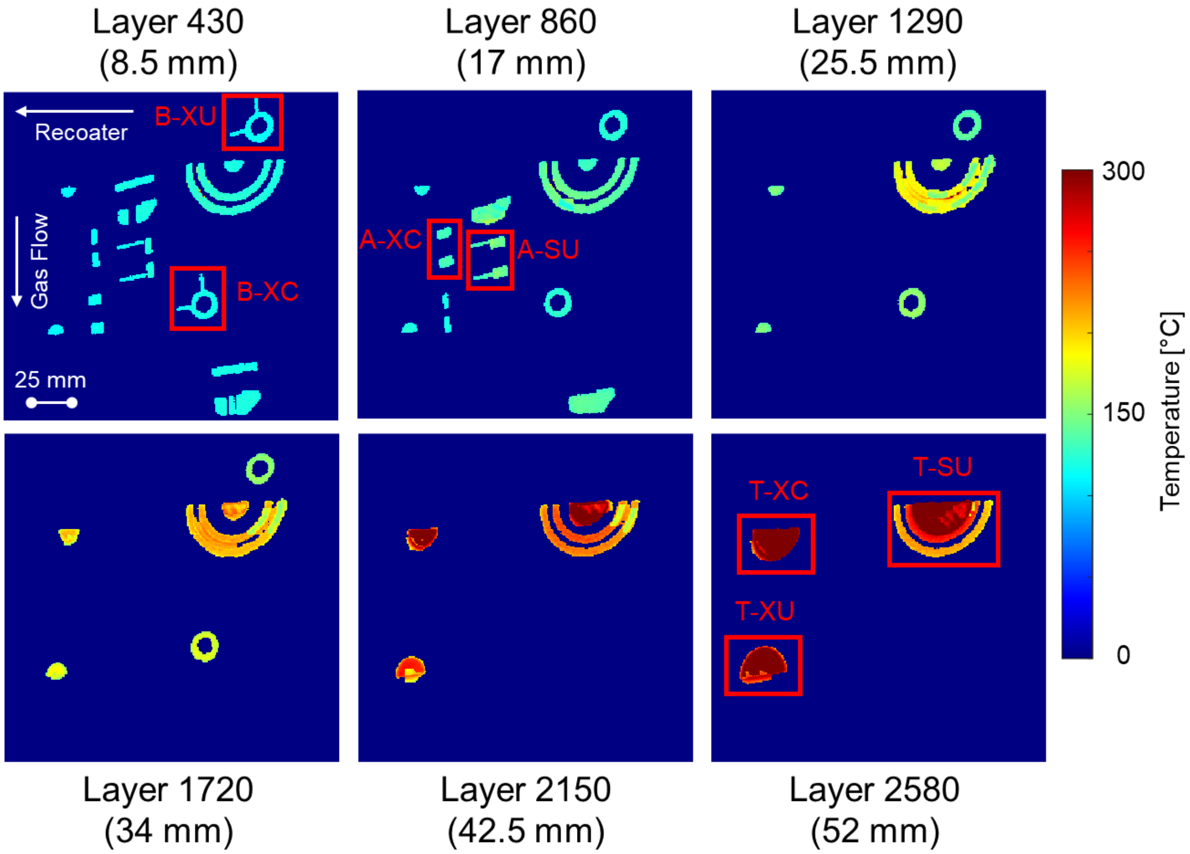

Figure 10: A composite end-of-cycle layer temperature for all parts on the build plate shown for select layers.

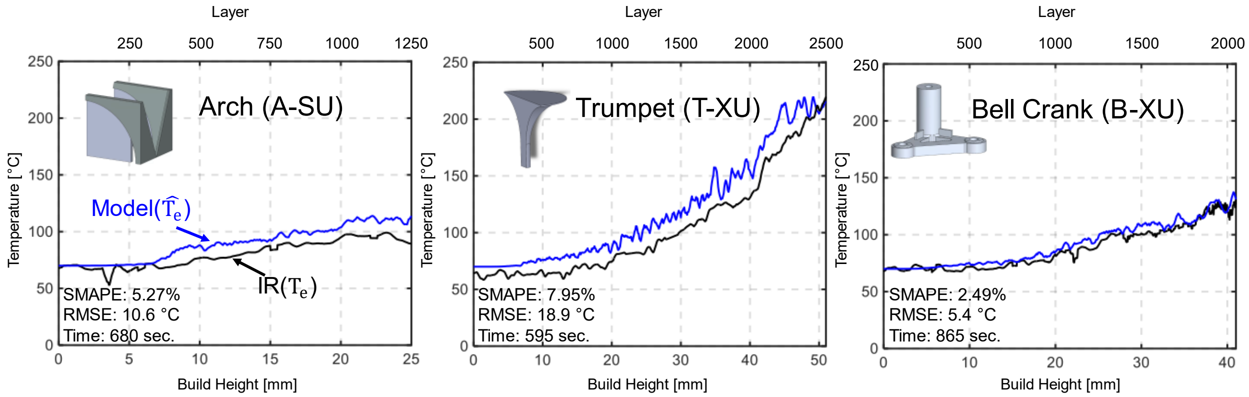

Figure 11: Comparision of the average end-of-cycle temperature predicted ($\hat{T}_e$) by the model for the supported arch (A-SU), unsupported trumpet (T-XU), and uncontrolled bell crank (B-XU). The model was able to predict part end-of-cycle temperature with a symmetric mean absolute percentage error ranging from 2.5% to 8%; and completed in ~15 minutes for the bell crank.

Table 2: Simulation parameters obtained after model calibration.

Simulation Parameters	Values
Heat loss coefficient part to powder, h_p [$W\cdot m^{-2}\cdot$ °C]	30
Heat loss coefficient part to substrate, h_s [$W\cdot m^{-2}\cdot$ °C]	20,000
Heat loss coefficient to gas flow, h_g [$W\cdot m^{-2}\cdot$ °C]	30
Thermal Conductivity (k) [$W\cdot m^{-1}\cdot$°C]	17
Density (ρ) [$kg\cdot m^{-3]}$	8,193
Specific Heat (c_p) [$J\cdot Kg^{-1}\cdot °C^{-1}$]	540
Melting Point (T_0) [°C]	1,609
Ambient chamber temperature, T_p [°C]	70
Node density [$nodes\cdot mm^3$]	1
Superlayer thickness [mm]	0.1 (5 actual layers)
Gain factor (*g*) [unitless]	0.6
Computational hardware	AMD Ryzen 3970X CPU, @3.70 GHz

5 Results

5.1 Arch

Shown in Figure 12(a) are the average end-of-cycle layer temperature predictions for the supported, uncontrolled arch (A-SU, $\widehat{T}_{\text{ideal}}$) and the unsupported arch printed with DynamicPrint (A-XC). The controller recommended layer-by-layer laser power plan is shown in Figure 12(b). These laser power changes were implemented by editing the default process parameters through the slicing software native to the LPBF machine (EOS Build). Also shown in Figure 12(a) is the hypothetical model predicted thermal history of an unsupported arch without control, which would result in overheating, and recoater crash. The laser power recommended by DynamicPrint tailored the thermal history of the unsupported, controlled arch (A-XC) to match that of the supported, uncontrolled arch (A-SU). Using the laser power plan recommended by DynamicPrint significantly reduced heat retention in A-XC. As shown in Figure 12(b), DynamicPrint reduced the laser power progressively to avoid overheating of the unsupported arch (A-XC). The computation time for DynamicPrint to converge was 35 minutes and the time to calculate a single iteration was 11 minutes.

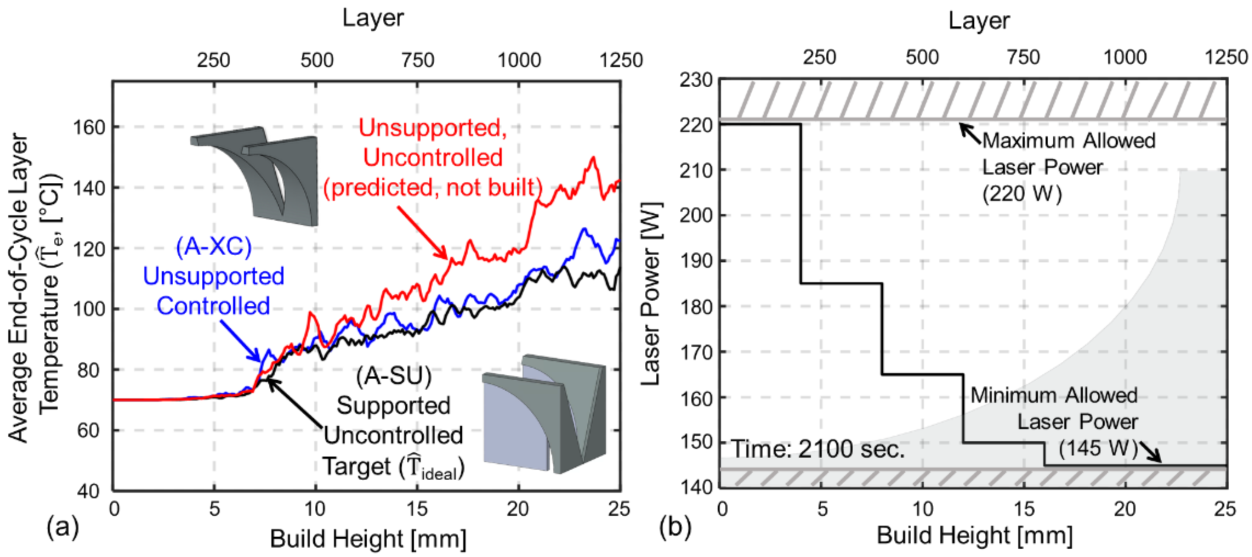

Figure 12: (a) The graph theory thermal predictions for the unsupported, controlled (A-XC, $\hat{T}_{original}$) and supported, uncontrolled (A-SU, $\hat{T}_{ideal}$) arches, and a hypothetical unsupported uncontrolled geometry. DynamicPrint MPC was able to closely match the thermal history of the unsupported arch (A-XC) to the supported arch (A-SU). (b) The recommended laser power settings for the unsupported, controlled part (A-XC) as a function of build height. DynamicPrint constrained the laser power between 145 W and 225 W.

In Figure 13, the 3D temperature distribution resulting from DynamicPrint are compared for all three arches in 4 mm epochs. In the case of the arch-shaped part (A-XU) built without supports under uncontrolled conditions, significant overheating is predicted in the overhang region. This overheating has been shown in previous works to result in part distortion and recoater crash [2, 58]. By contrast, altering the laser power during printing of an unsupported, controlled arch (A-XC) to best match the thermal history of the supported, uncontrolled arch (A-SU) greatly reduces heat accumulation. The temperature distribution of the unsupported, controlled arch (A-XC) does not exactly match the thermal history of the supported arch A-SU ($\hat{T}_{\text{ideal}}$), because the laser power is constrained between 145 W and 225 W to prevent porosity formation.

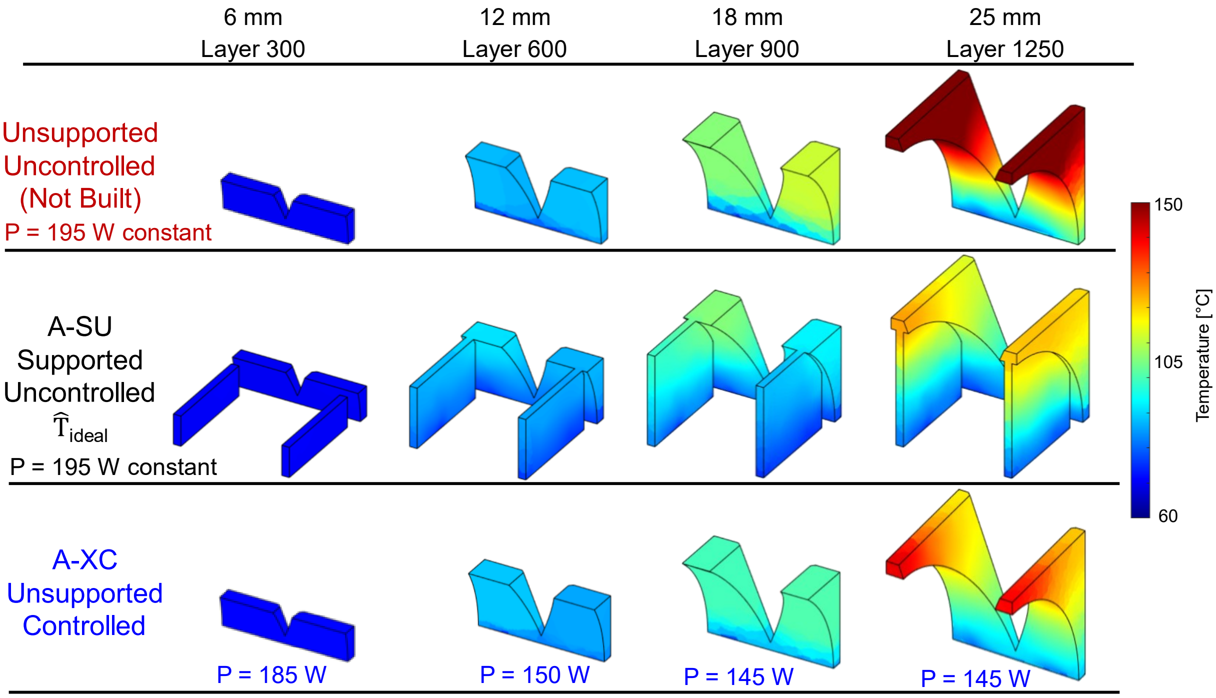

Figure 13: End-of-cycle thermal predictions for four selected build layers of the three arch-shaped parts created in this work. By changing the laser power based on the MPC, the thermal history of the unsupported, controlled arch (A-XC) closely matched the thermal history of the supported, uncontrolled geometry (A-SU). By contrast, the unsupported, uncontrolled arch is predicted to overheat, and potentially lead to a recoater crash.

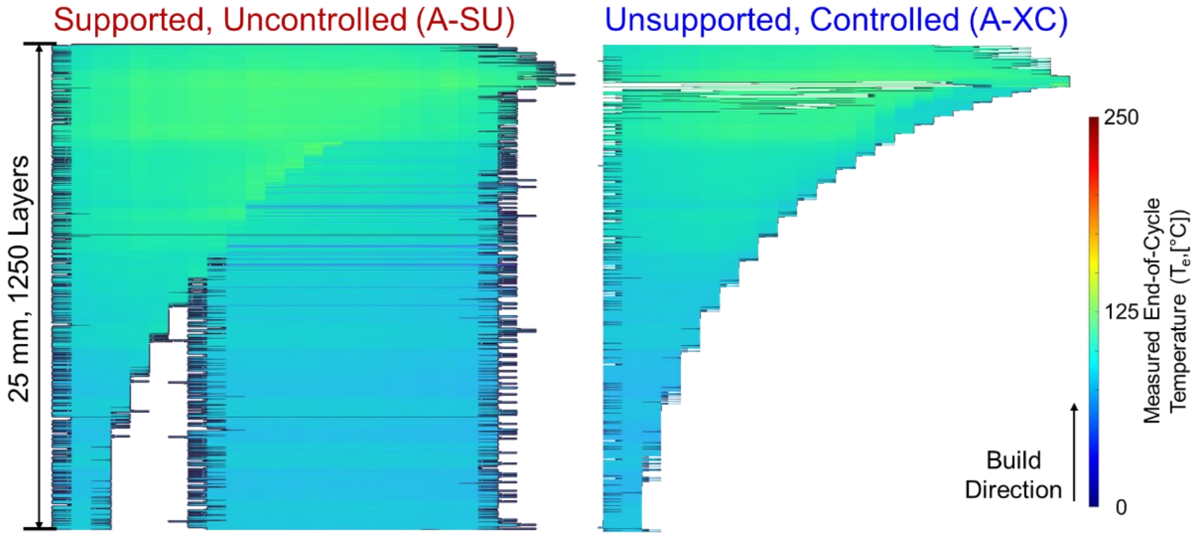

Figure 14: Composite image comparison of the end-of-cycle layer temperature for the arch geometries as observed by the IR camera. Applying DynamicPrint for the unsupported arch results in a nearly identical thermal distriubution as the supported arch.

Figure 14 is a composite image of the average end-of-cycle layer temperature (T_e) measured from the IR camera along the build direction. The edges of the image are imprecise due to blurring of thermal images around the boundary of the part. The IR data affirms the reduced heat retention in the unsupported, controlled arch (A-XC), and that its thermal history closely matches that of the ideal supported, uncontrolled arch (A-SU).

A comparison of the X-ray CT images of the two arch-shaped parts, A-SU and A-XC, is shown in Figure 15. Here the parts are viewed in the XZ plane to ascertain their magnitude of distortion. In Figure 15, moderate levels of geometric deviation were observed above 22 mm build height for both parts. This deviation is to be expected and often occurs when creating the extreme overhang at the top of the part [2, 58]. Deviation in the unsupported, controlled arch (A-XC) was successfully mitigated until the same build height as the supported, uncontrolled arch (A-SU), and their magnitudes of deviation were similar. Thus, DynamicPrint was able to limit geometric deviation to a magnitude comparable to that of the supported geometry. Consequently, practitioners can eliminate recoater crashes, as well as delete support structures in complex overhang structures.

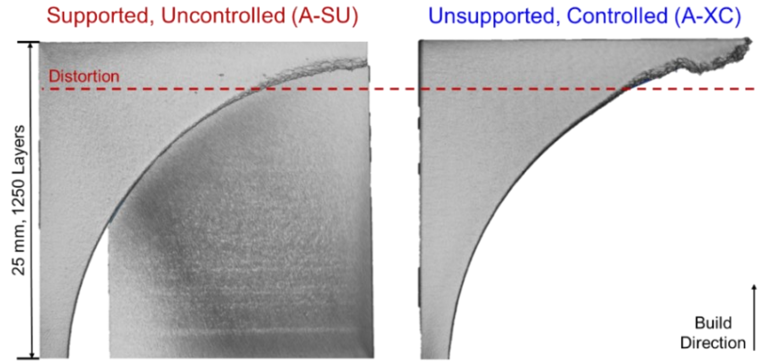

Figure 15: X-ray CT comparison of the supported, uncontrolled (A-SU) and unsupported, controlled (A-XC) arch parts. DynamicPrint successfully created the arch without support (A-XC) with the same magnitude of distortion as that of the supported, uncontrolled arch (A-SU). Thus, saving on the effort and time required to remove support structures. The dotted line indicates the region (~ 22 mm) where similar levels of geometric deviation were observed in A-SU and A-XC.

After X-ray CT analysis, the parts were cut, polished, and etched with aqua regia (3:1, HCl: HNO_3). The microstructure was subsequently analyzed using scanning electron microscopy. The resulting primary dendritic arm spacing (PDAS, λ_1) measured at three locations along the build direction of the parts is shown in Figure 16. Except for the location 1 in Figure 16, the PDAS measured in unsupported, controlled arch (A-XC) was statistically similar to the PDAS observed for the supported, uncontrolled arch (A-SU). Indeed, the PDAS for A-XC is consistent in the range of 400 ± 50 nm throughout.

Similarity in PDAS of A-XC and A-SU is to be expected and desired as the thermal history of A-XC was tailored to match the supported, uncontrolled arch A-SU. The discrepancy in location 1 is likely due to heat sink effect of the substrate and support structures that results in rapid cooling of initial layers. Thus, DynamicPrint facilitates elimination of support structures, while maintaining consistency of microstructure and not degrading the geometric integrity. Wide field-of-view SEM images were acquired at several locations, representative images are shown in Figure 17; neither lack-of-fusion porosity or keyhole porosity were observed in these SEM images.

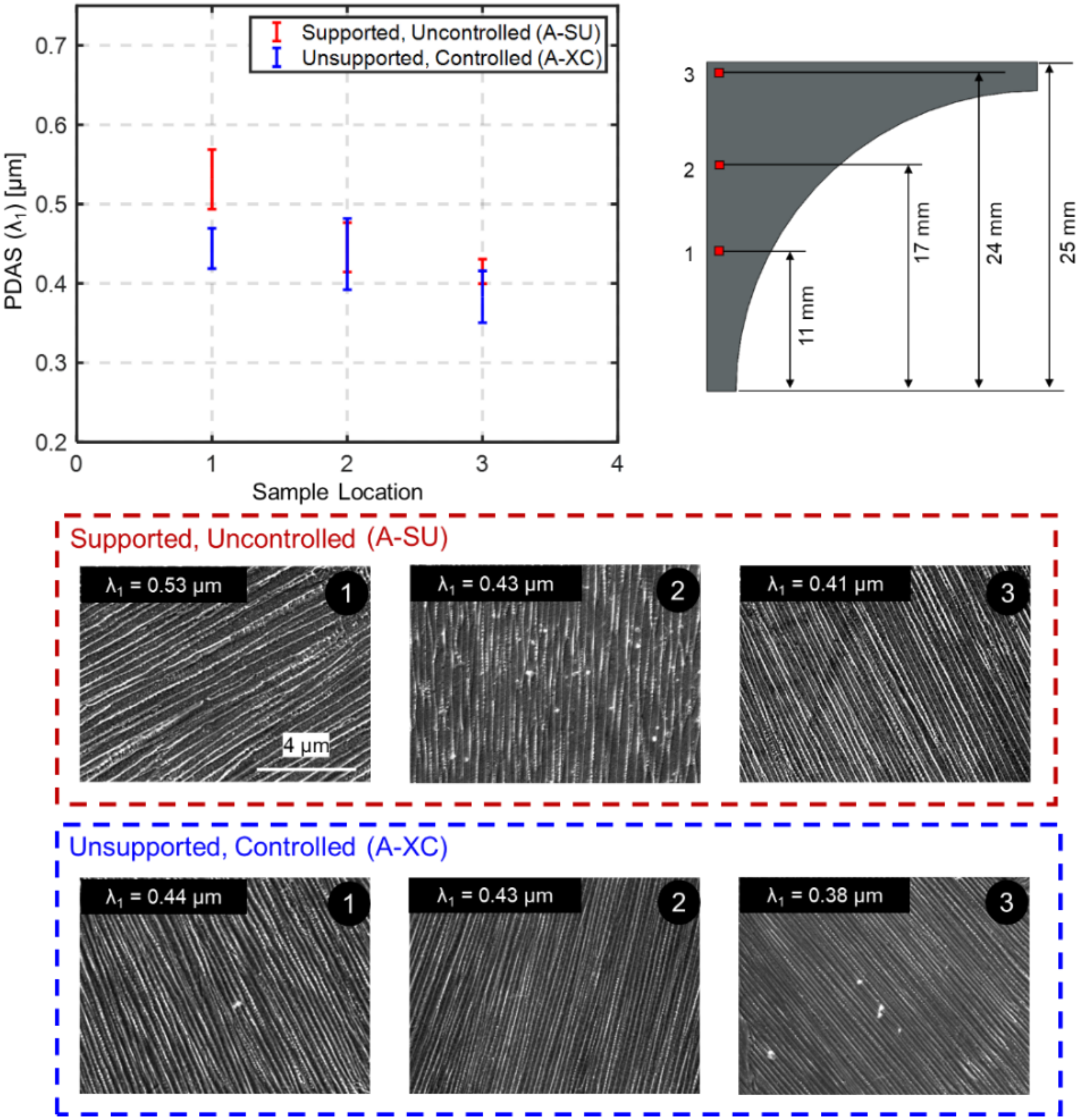

Figure 16*: (Top) Primary dendritic arm spacing (PDAS, λ_1) measurements taken at three sample locations in the arch parts. The PDAS of the unsupported, controlled arch was similar to the supported, uncontrolled arch. (Bottom) Representative SEM micrographs at three locations.*

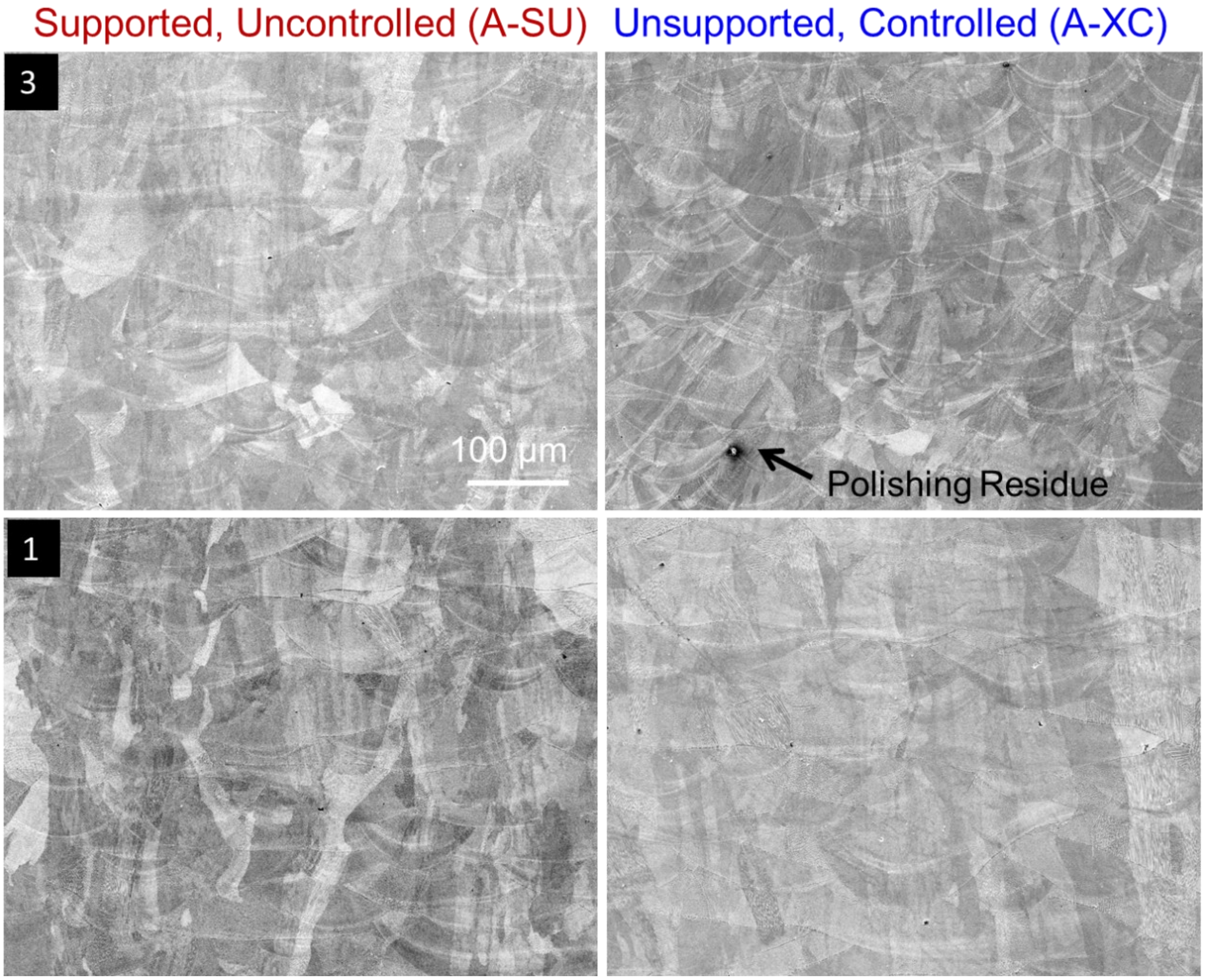

Figure 17:Representative wide field-of-view SEM images at two locations for the arch-shaped parts A-SU and A-XC referenced in Figure 16. No lack-of-fusion or key hole pores were observed.

5.2 Trumpet

Akin to the arch-shaped parts, the trumpet-shaped part has a progressively increasing overhang feature over a relatively tall build height of 52 mm (2600 layers). Shown in Figure 18(a) are the model predicted average layer end-of-cycle temperature ($\widehat{\mathrm{T}}_e$) for the unsupported, uncontrolled (T-XU, $\hat{T}_{orignial}$); supported, uncontrolled (T-SU, $\widehat{\mathrm{T}}_{\mathrm{ideal}}$); and the unsupported, controlled (T-XC) geometries. The trumpet T-XU tends to retain heat, with the average end-of-cycle layer temperature reaching ~ 200 °C near the top of the part. In T-SU, the support structures mitigate heat accumulation, by providing a conductive pathway for the heat to flow to the substrate.

The aim of DynamicPrint was to adjust the laser power such that the thermal history of T-XC would match the thermal history of T-SU. In other words, the target ($\widehat{\mathrm{T}}_{\mathrm{ideal}}$) end-of-cycle temperature for T-XC was the average end-of-cycle temperature of T-SU. As shown in Figure 18(a) and (b), the DynamicPrint approach successfully restrains the heat accumulation in T-XC by progressively reducing the laser power layer-by-layer. The computation time for DynamicPrint to obtain the processing parameters shown in Figure 18(b) was 220 minutes. The simulation time of a single iteration was 10 minutes.

The 3D model-predicted temperature distribution for T-XU and T-XC geometries are presented in Figure 18 for 12.5 mm build height intervals. These predictions are affirmed in the IR-measured end-of-cycle temperature (T_e) composite images of T-XU and T-XC depicted in Figure 19, which show that the DynamicPrint successfully mitigated heat accumulation in the top layers of the trumpet T-XC.

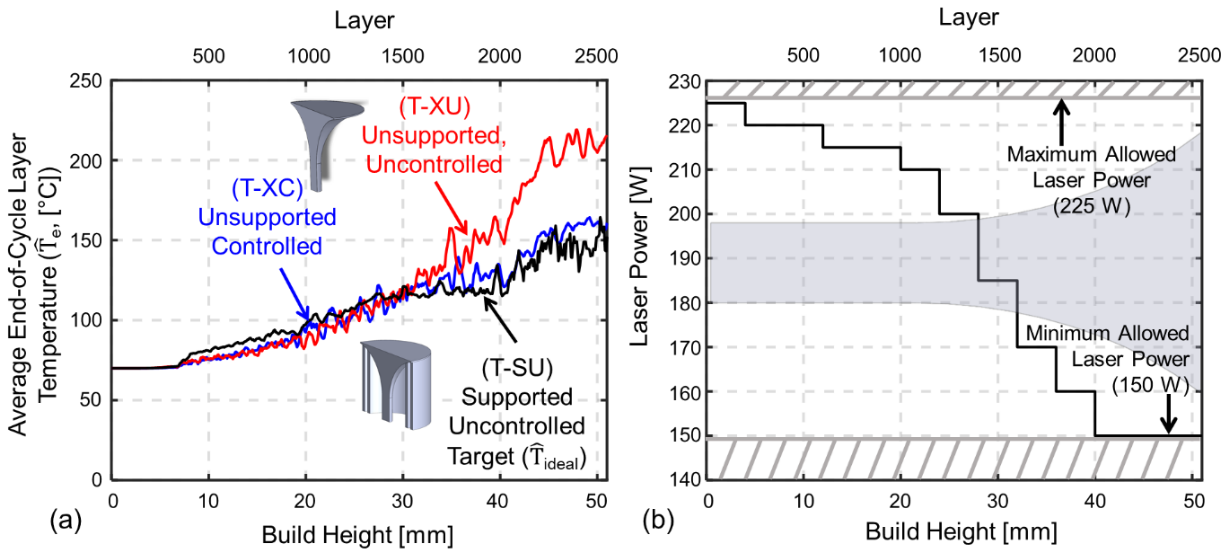

Figure 18: (a) The graph theory thermal predictions for the three uncontrolled and controlled trumpet geometries. The DynamicPrint approach was able to alter process parameters to closely match the mean surface temperature of the supported geometry, resulting in reduced overheating in the unsupported, controlled (T-XC) geometry. (b) The laser power settings derived by DynamicPrint strategy.

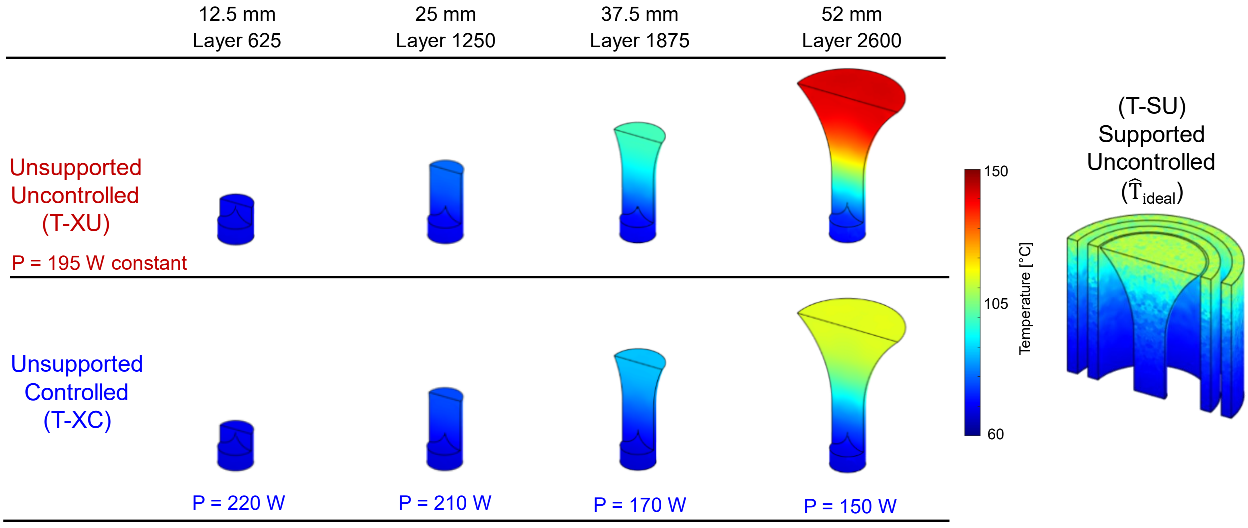

Figure 19: Comparison of the predicted temperature disbribution for the unsupported, uncontrolled (T-XU) and unsupported, controlled (T-XC) geometetries, along with the ideal supported, uncontrolled geometry (T-SU). DynamicPrint significantly reduced overheating in the trumpet part compared to the uncontrolled trumpet.

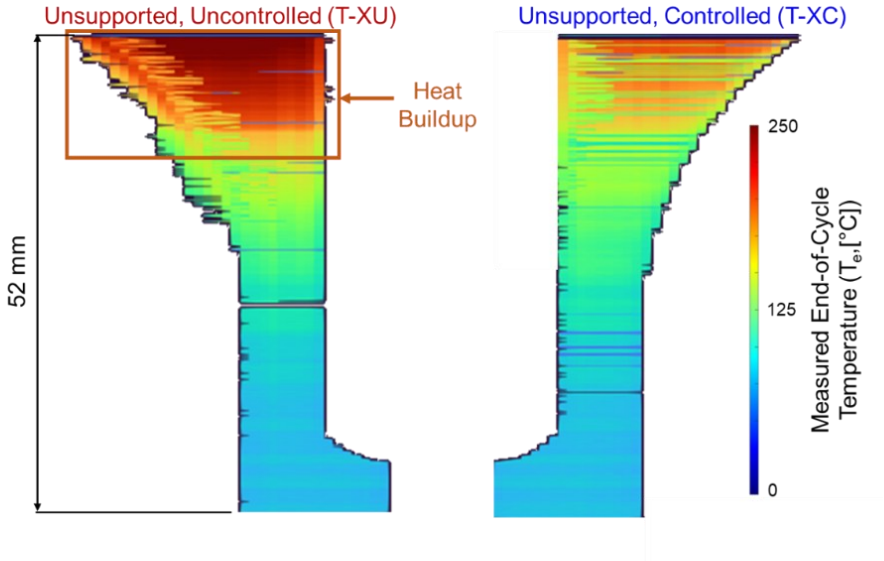

Figure 20: Comparison of the end-of-cycle temperature for the trumpet geometries. Process control of thermal history significantly reduced heat accumulation in the top section of the part.

Next, the primary dendritic arm spacing (PDAS, λ_1) of T-XU and T-XC trumpet geometries were analyzed. The PDAS measurements were obtained at nine locations along the build height. Representative SEM micrographs at four of these locations are shown in Figure 20. The PDAS of T-XC is discernably smaller than that of T-XU. This reduction in PDAS is symptomatic of reduced heat accumulation and faster cooling rates as shown in our previous work [19].

Continuing with the analysis, in Figure 22(a) the PDAS measurements for T-XC and T-XU are plotted at nine locations along the build height. The PDAS for T-XU ranged from 500 nm to 690 nm. In comparison, the PDAS for T-XC ranged from 350 nm to 400 nm. Further, T-SU ranged from 390 to 690 nm. As evident from Figure 22(b), the larger variation in PDAS of T-XU translates to larger variation in microhardness (Vickers microhardness, $HV_{0.3,10}$). Whilst the mean microhardness for T-XC and T-XU cases was statistically identical, the standard deviation in microhardness for T-XU was 9.5 HV compared to 5.3 HV for T-XC. We note that although the support structures in T-SU reduced the standard deviation of microhardness to 7.7 HV, however this reduction requires removal of supports and increases part cost. Wide field-of-view SEM images were acquired for the three trumpet-shaped parts. Representative images are shown in Figure 23; lack-of-fusion or keyhole pores are not evident in these SEM images.

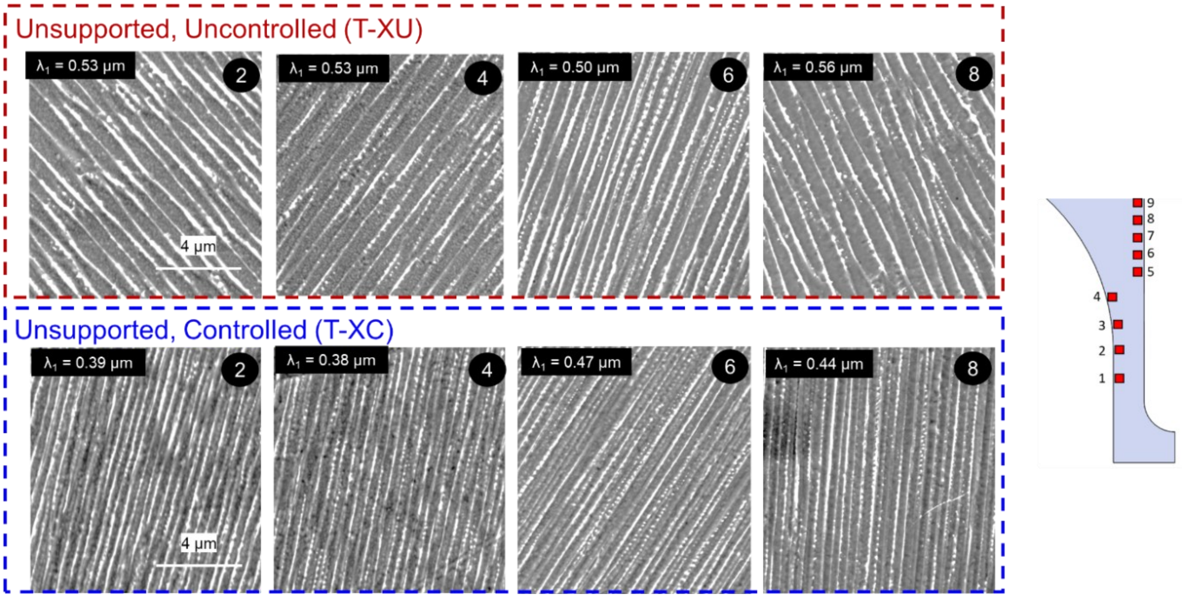

Figure 21: Scanning electron microscopy images comparing the primary dendritic arm spacing (PDAS, λ1) measurements for the unsupported, uncontrolled (T-XU) and unsupported, controlled (T-XC) trumpet geometries. The PDAS was measured at 9 locations along the build height. The PDAS for T-XU is noticably larger compared to T-XC.

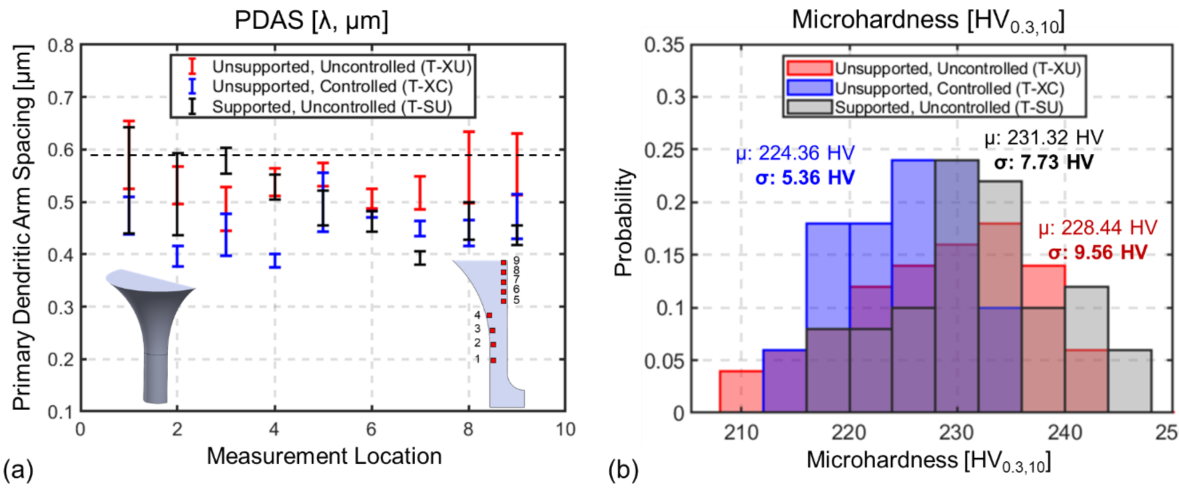

Figure 22: (a) Comparision of the PDAS for the unsupported, uncontrolled (T-XU), unsupported, controlled (T-XC), and supported, controlled trumpet (T-SU). The variation in PDAS is significantly reduced for the controlled trumpet. (b) The large variation in PDAS for the uncontrolled trumpet results in large viariation in microhardness.

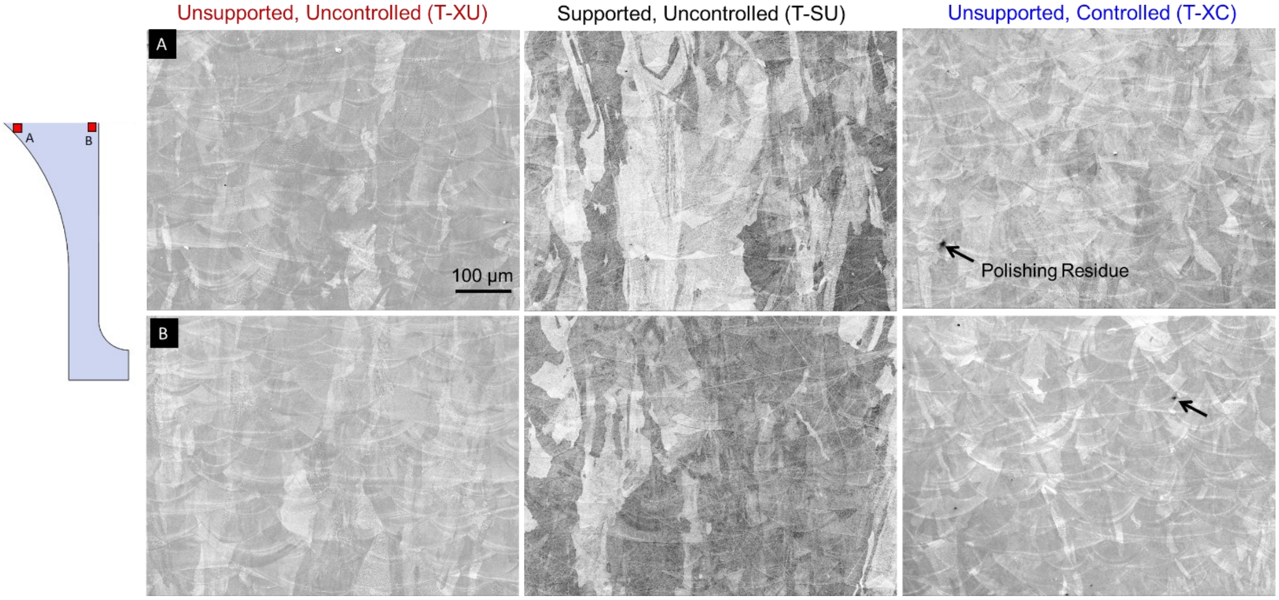

Figure 23:Representative wide field-of-view SEM images at two locations for the trumpet-shaped parts T-XU, T-SU, T-XC. No lack-of-fusion or key hole pores were observed.

5.3 Bell Crank

The thermal history predictions for the uncontrolled (B-XU) and controlled (B-XC) bell crank geometries are presented in Figure 24 and Figure 25. Here the target thermal history ($\widehat{\mathrm{T}}_{\mathrm{ideal}}$) was to maintain a constant average end-of-cycle layer temperature $\widehat{\mathrm{T}}_{\mathrm{e}}$ = 75 °C after 7 mm of build height, which corresponded to the temperature when the base section of the part was completed. The layer-wise power adjustments suggested by the controller are presented in Figure 24(b). The model predicted control strategy converged within 320 minutes with a single iteration computation time of 15 minutes. Shown in Figure 25 is the 3D model predicted temperature distribution for B-XU and B-XC at approximately 10 mm intervals.

These results demonstrate that compared to B-XU, heat retention in B-XC was considerably reduced on account of DynamicPrint, especially towards the last 15 mm of the build. The reduced heat accumulation and relatively homogenous thermal history of B-XC in comparison to B-XU is further affirmed from the infrared average end-of-cycle layer temperature composite image presented in Figure 26. However, the controller could not completely eliminate heat retention and achieve the targeted constant average end-of-cycle layer temperature of 80 °C. This is because, as evident in Figure 24(b), the minimal permissible laser power was set to 145 W to avoid lack-of-fusion porosity. Despite this constraint, as reported in Figure 24(a), the resulting $\widehat{\mathrm{T}}_{\mathrm{e}}$ of B-XC drifts at the most 30 °C from the target temperature of 80 °C, in comparison for B-XU, the deviation in $\widehat{\mathrm{T}}_{\mathrm{e}}$ from the setpoint is as large as 60 °C.

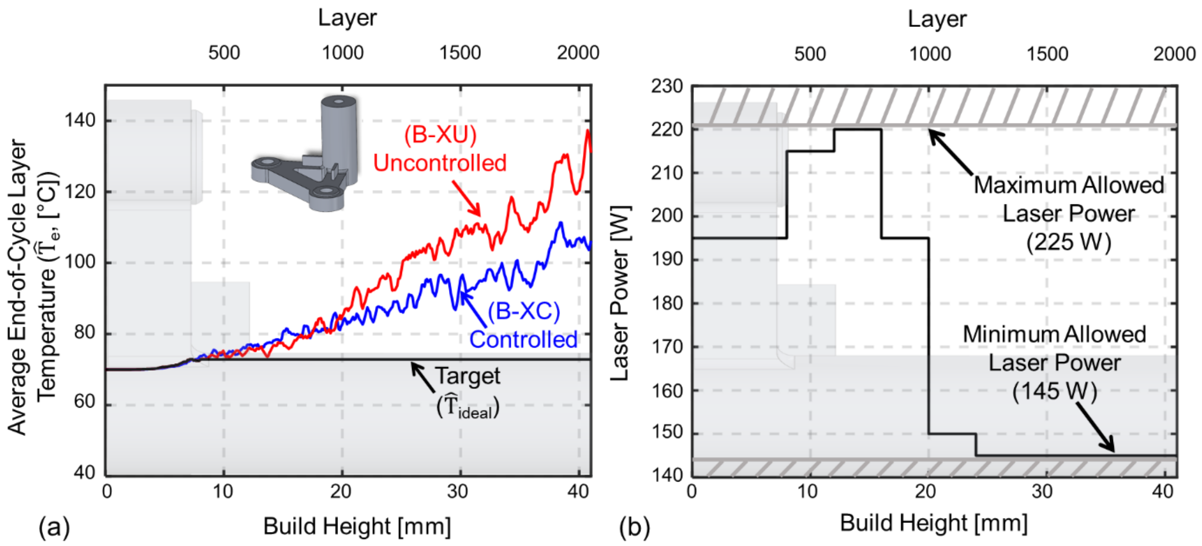

Figure 24: (a) The graph theory thermal predictions for the uncontrolled (B-XU) and controlled (B-XC) bell crank parts. The target thermal history ($\hat{T}_{ideal}$) is a uniform temperature of 75 °C. DynamicPrint reduced overheating and created a temperature distribution closer to the identified $\hat{T}_{ideal}$. Due to constraints placed on the laser power, not all heat accumulation could be eliminated. (b) The process parameters recommended by DynamicPrint, within the laser power constraints of 145 W and 225 W.

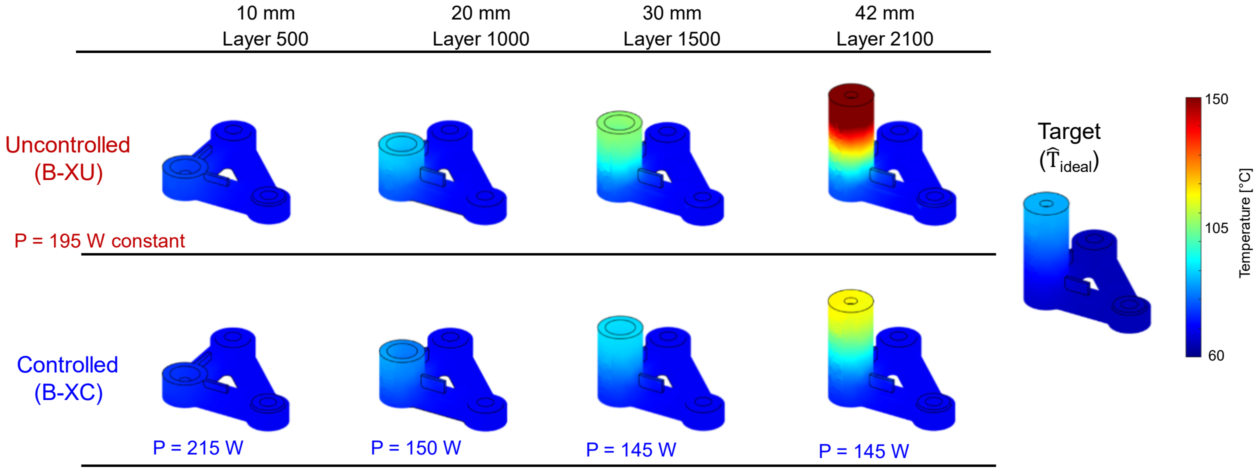

Figure 25: End-of-cycle temperature predictions for the uncontrolled (B-XU) and controlled (B-XC) bell crank geometries for four selected build layers. Model predictive process control mitigates heat accumulation.

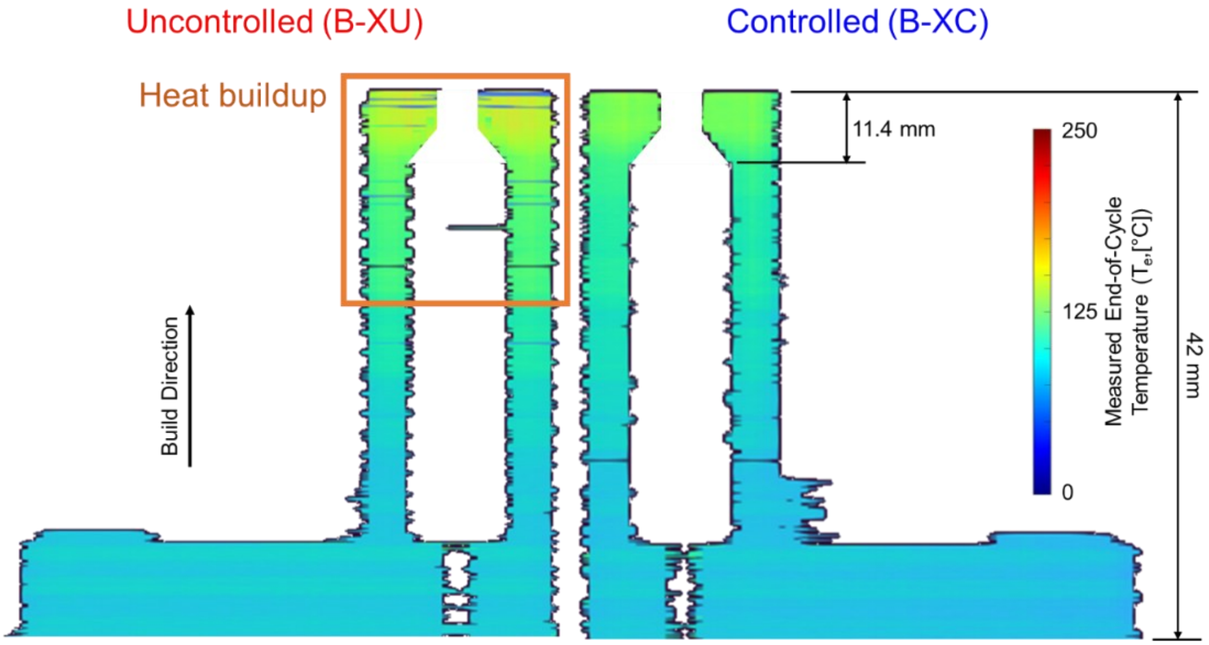

Figure 26: Composite image comparison of the end-of-cycle layer temperature for the bell crank geometries as observed by the IR camera. Model predictive process control of thermal history significantly reduced heat accumulation in the top section of the part.

Shown in Figure 27 are X-ray CT images for B-XU and B-XC in the X-Z and X-Y planes. X-ray CT analysis reveals that the reduction in heat accumulation of B-XC considerably improved geometric resolution and surface integrity of internal features. Along the build direction, the corners at the topmost section of B-XC are notably sharper compared to B-XU. Similarly, in the X-Y cross-section images located at 35 mm and 39 mm, rougher boundaries for B-XU are visually evident compared to B-XC. Noting that the interior of the part has powder trapped within it, the increased heat accumulation near the top in the case of B-XU results in partial melting of the powder particles in contact with the interior walls. These geometry and surface-related anomalies in the internal overhang feature would require specialized tooling to correct post-process using machining.

These geometry integrity-related improvements were quantified by pixel analysis of X-ray CT cross-section images. The diameter variation for the interior overhang feature as a function of layer height is shown in Figure 28(a). In the uncontrolled bell crank (B-XU), the uneven temperature distribution causes increased deviation from the designed dimensions. The internal channel of B-XU is oversized by as much as 0.5 mm from the designed dimensions. The standard deviation of the size of the internal channel is reported in Figure 28(b). The diameter of B-XU has a standard deviation ranging from 50 μm to 450 μm, compared to 100 μm for B-XC. In the context of the bell crank geometry, DynamicPrint improves the surface integrity and geometric accuracy of difficult to post-process internal features, with implications to functional integrity, such as fatigue life [76]. Lastly, no lack-of-fusion pores were observed in the X-ray CT images obtained for the controlled bell crank part.

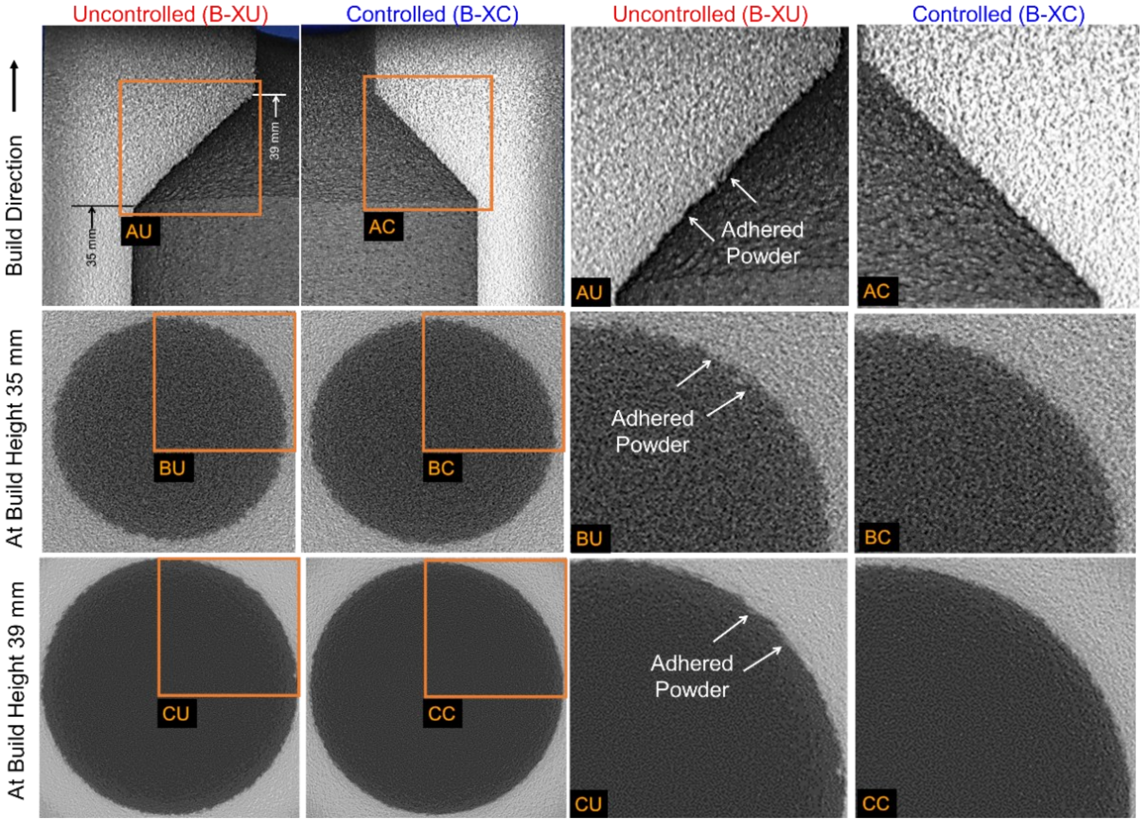

Figure 27: X-Ray CT scans of the inner diameters of the controlled (B-XC) and uncontrolled (B-XU) bell crank parts. Note the adhered powder in B-XU on account of over sintering due to heat accumulation. The controlled geometry (B-XC) portrays an improved surface integrity, on account of minimal adhered powder than the uncontrolled (B-XU).

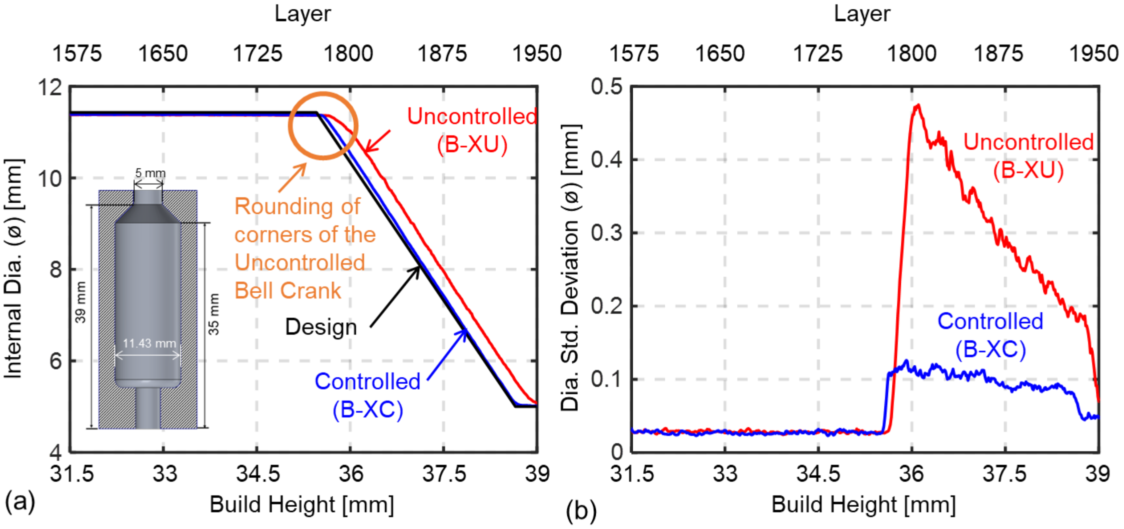

Figure 28: X-Ray CT of geometric deviation comparison between the uncontrolled (B-XU) and controlled (B-XC) bell crank parts. (a) Inner diameter of the internal overhang feature of the bell crank parts. DynamicPrint resulted in an internal geometry closer to the design dimensions. (b) Diameter standard deviation of the bell cranks for the overhang region. The higher standard deviation in the internal diameter for B-XU is a result of heat retention.

6 Conclusions and Future Works

We established a physics-based process control approach termed *DynamicPrint* to mitigate thermal-induced defect formation in laser powder bed fusion (LPBF). Starting with part shape, material properties, and manufacturer-recommended processing parameters, DynamicPrint autonomously adjusts the parameters layer-by-layer before the LPBF part is printed to avoid non-uniform temperature distributions that often lead to defects at multiple scales. DynamicPrint thus offers a rapid, physics-based pathway for process qualification, which can potentially accelerate the time-to-market of LPBF parts, as opposed to the existing cumbersome and expensive empirical build-and-test approach. Specific outcomes from this work are as follows.

1) DynamicPrint was applied to three complex shapes: an arch, trumpet, and bell crank. These geometries included challenging features such as steep overhangs and internal channels with undercuts. The approach successfully adjusted the processing parameters layer-by-layer for each of these geometries within 3 to 6 hours on a desktop PC.
2) In the arch- and trumpet-shaped parts with steep overhang features the layer-wise adjustment of process parameters implemented by DynamicPrint eliminated recoater crashes, as well as enabled printing of such parts without supports. This can enhance process yield, save several hours of machining and post-processing time, as well as reduce material usage. Additionally, the trumpet-shaped part produced with DynamicPrint showed consistent grain size and reduced variation in microhardness. X-ray CT analysis and SEM micrographs confirmed that the parts were fully dense, with no evidence of lack-of-fusion or keyhole porosity.
3) The DynamicPrint approach was also applied to a complex bell crank geometry with an internal channel that is difficult to finish machine. Compared to the bell crank part built with

constant laser power settings, the part built with DynamicPrint had significantly improved surface integrity and geometric resolution, beneficial for fatigue life.

In our future works, we will expand the DynamicPrint approach beyond the current layer-wise control to within-layer control.

References

[1] A. Ashby, G. Guss, R.K. Ganeriwala, A.A. Martin, P.J. DePond, D.J. Deane, M.J. Matthews, C.L. Druzgalski, Thermal history and high-speed optical imaging of overhang structures during laser powder bed fusion: A computational and experimental analysis, Additive Manufacturing 53 (2022) 102669. doi: https://doi.org/10.1016/j.addma.2022.102669

[2] R. Yavari, Z. Smoqi, A. Riensche, B. Bevans, H. Kobir, H. Mendoza, H. Song, K. Cole, P. Rao, Part-scale thermal simulation of laser powder bed fusion using graph theory: Effect of thermal history on porosity, microstructure evolution, and recoater crash, Materials & Design 204 (2021) 109685. doi: https://doi.org/10.1016/j.matdes.2021.109685

[3] B. Blakey-Milner, P. Gradl, G. Snedden, M. Brooks, J. Pitot, E. Lopez, M. Leary, F. Berto, A. du Plessis, Metal additive manufacturing in aerospace: A review, Materials & Design 209 (2021) 110008. doi: https://doi.org/10.1016/j.matdes.2021.110008

[4] T.W. Teasley, C.S. Protz, A.P. Larkey, B.B. Williams, P.R. Gradl, A Review Towards the Design Optimization of High Performance Additively Manufactured Rotating Detonation Rocket Engine Injectors, AIAA Propulsion and Energy 2021 Forum, American Institute of Aeronautics and Astronautics 2021.

[5] B. Ridgeway, NASA's 3D-printed Rotating Detonation Rocket Engine Test a Success, 2023. https://www.nasa.gov/centers-and-facilities/marshall/nasas-3d-printed-rotating-detonation-rocket-engine-test-a-success/. (Accessed 2/15/2024.

[6] Z. Snow, A.R. Nassar, E.W. Reutzel, Invited Review Article: Review of the formation and impact of flaws in powder bed fusion additive manufacturing, Additive Manufacturing 36 (2020) 101457. doi: https://doi.org/10.1016/j.addma.2020.101457

[7] M. Shahwaz, P. Nath, I. Sen, A critical review on the microstructure and mechanical properties correlation of additively manufactured nickel-based superalloys, Journal of Alloys and Compounds 907 (2022) 164530. doi: https://doi.org/10.1016/j.jallcom.2022.164530

[8] W.H. Kan, L.N.S. Chiu, C.V.S. Lim, Y. Zhu, Y. Tian, D. Jiang, A. Huang, A critical review on the effects of process-induced porosity on the mechanical properties of alloys fabricated by laser powder bed fusion, Journal of Materials Science 57(21) (2022) 9818-9865. doi: 10.1007/s10853-022-06990-7

[9] K.S. Stopka, A. Desrosiers, T. Nicodemus, N. Krutz, A. Andreaco, M.D. Sangid, Intentionally seeding pores in additively manufactured alloy 718: Process parameters, microstructure, defects, and fatigue, Additive Manufacturing 66 (2023) 103450. doi: https://doi.org/10.1016/j.addma.2023.103450

[10] A. Leicht, C. Pauzon, M. Rashidi, U. Klement, L. Nyborg, E. Hryha, Effect of part thickness on the microstructure and tensile properties of 316L parts produced by laser powder bed fusion, Advances in Industrial and Manufacturing Engineering 2 (2021) 100037. doi: https://doi.org/10.1016/j.aime.2021.100037

[11] W.J. Sames, F.A. List, S. Pannala, R.R. Dehoff, S.S. Babu, The metallurgy and processing science of metal additive manufacturing, International Materials Reviews 61(5) (2016) 315-360. doi: https://doi.org/10.1080/09506608.2015.1116649

[12] F. Nahr, M. Rasch, C. Burkhardt, J. Renner, B. Baumgärtner, T. Hausotte, C. Körner, P. Steinmann, J. Mergheim, M. Schmidt, M. Markl, Geometrical Influence on Material Properties for Ti6Al4V Parts in Powder Bed Fusion, Journal of Manufacturing and Materials Processing, 2023.

[13] T.G. Spears, S.A. Gold, In-process sensing in selective laser melting (SLM) additive manufacturing, Integrating Materials and Manufacturing Innovation 5(1) (2016) 16-40. doi: https://doi.org/10.1186/s40192-016-0045-4

[14] J.P. Oliveira, A.D. LaLonde, J. Ma, Processing parameters in laser powder bed fusion metal additive manufacturing, Materials & Design 193 (2020) 108762. doi: https://doi.org/10.1016/j.matdes.2020.108762

[15] S.R. Narasimharaju, W. Zeng, T.L. See, Z. Zhu, P. Scott, X. Jiang, S. Lou, A comprehensive review on laser powder bed fusion of steels: Processing, microstructure, defects and control methods, mechanical properties, current challenges and future trends, Journal of Manufacturing Processes 75 (2022) 375-414. doi: https://doi.org/10.1016/j.jmapro.2021.12.033

[16] A.D. Peralta, M. Enright, M. Megahed, J. Gong, M. Roybal, J. Craig, Towards rapid qualification of powder-bed laser additively manufactured parts, Integrating Materials and Manufacturing Innovation 5(1) (2016) 154-176. doi: 10.1186/s40192-016-0052-5

[17] G. Mohr, S.J. Altenburg, K. Hilgenberg, On the limitations of small cubes as test coupons for process parameter optimization in laser powder bed fusion of metals, Journal of Laser Applications 35(4) (2023). doi: https://doi.org/10.2351/7.0001080

[18] A. Riensche, B.D. Bevans, Z. Smoqi, R. Yavari, A. Krishnan, J. Gilligan, N. Piercy, K. Cole, P. Rao, Feedforward control of thermal history in laser powder bed fusion: Toward physics-based optimization of processing parameters, Materials & Design 224 (2022) 111351. doi: https://doi.org/10.1016/j.matdes.2022.111351

[19] A.R. Riensche, B.D. Bevans, G. King, A. Krishnan, K.D. Cole, P. Rao, Predicting meltpool depth and primary dendritic arm spacing in laser powder bed fusion additive manufacturing using physics-based machine learning, Materials & Design 237 (2024) 112540. doi: https://doi.org/10.1016/j.matdes.2023.112540

[20] R. Yavari, A. Riensche, E. Tekerek, L. Jacquemetton, H. Halliday, M. Vandever, A. Tenequer, V. Perumal, A. Kontsos, Z. Smoqi, K. Cole, P. Rao, Digitally twinned additive manufacturing: Detecting flaws in laser powder bed fusion by combining thermal simulations with in-situ meltpool sensor data, Materials & Design 211 (2021) 110167. doi: https://doi.org/10.1016/j.matdes.2021.110167

[21] C.-J. Bae, A.B. Diggs, A. Ramachandran, 6 - Quantification and certification of additive manufacturing materials and processes, in: J. Zhang, Y.-G. Jung (Eds.), Additive Manufacturing, Butterworth-Heinemann2018, pp. 181-213.

[22] C.L. Druzgalski, A. Ashby, G. Guss, W.E. King, T.T. Roehling, M.J. Matthews, Process optimization of complex geometries using feed forward control for laser powder bed fusion additive manufacturing, Additive Manufacturing 34 (2020) 101169. doi: https://doi.org/10.1016/j.addma.2020.101169

[23] M. Seifi, A. Salem, J. Beuth, O. Harrysson, J.J. Lewandowski, Overview of Materials Qualification Needs for Metal Additive Manufacturing, JOM 68(3) (2016) 747-764. doi: 10.1007/s11837-015-1810-0

[24] Y. Huang, M.C. Leu, J. Mazumder, A. Donmez, Additive Manufacturing: Current State, Future Potential, Gaps and Needs, and Recommendations, Journal of Manufacturing Science and Engineering 137(1) (2015). doi: 10.1115/1.4028725

[25] K.D. Cole, A. Riensche, P.K. Rao, Discrete Green's functions and spectral graph theory for computationally efficient thermal modeling, International Journal of Heat and Mass Transfer 183 (2022) 122112. doi: https://doi.org/10.1016/j.ijheatmasstransfer.2021.122112

[26] M. Schwenzer, M. Ay, T. Bergs, D. Abel, Review on model predictive control: an engineering perspective, The International Journal of Advanced Manufacturing Technology 117(5-6) (2021) 1327-1349. doi: https://doi.org/10.1007/s00170-021-07682-3

[27] T.P. Moran, P. Li, D.H. Warner, N. Phan, Utility of superposition-based finite element approach for part-scale thermal simulation in additive manufacturing, Additive Manufacturing 21 (2018) 215-219. doi: https://doi.org/10.1016/j.addma.2018.02.015

[28] N. Peter, Z. Pitts, S. Thompson, A. Saharan, Benchmarking build simulation software for laser powder bed fusion of metals, Additive Manufacturing 36 (2020) 101531. doi: https://doi.org/10.1016/j.addma.2020.101531

[29] F. Dugast, P. Apostolou, A. Fernandez, W. Dong, Q. Chen, S. Strayer, R. Wicker, A.C. To, Part-scale thermal process modeling for laser powder bed fusion with matrix-free method and GPU computing, Additive Manufacturing 37 (2021) 101732. doi: https://doi.org/10.1016/j.addma.2020.101732

[30] A. Olleak, F. Dugast, P. Bharadwaj, S. Strayer, S. Hinnebusch, S. Narra, A.C. To, Enabling Part-Scale Scanwise process simulation for predicting melt pool variation in LPBF by combining GPU-based Matrix-free FEM and adaptive Remeshing, Additive Manufacturing Letters 3 (2022) 100051. doi: https://doi.org/10.1016/j.addlet.2022.100051

[31] K.S. Ramani, C. He, Y.-L. Tsai, C.E. Okwudire, E. Malekipour, SmartScan: An intelligent scanning approach for uniform thermal distribution, reduced residual stresses and deformations in PBF additive manufacturing, Additive Manufacturing 52 (2022) 102643. doi: https://doi.org/10.1016/j.addma.2022.102643

[32] X. Li, N. Polydorides, Time-efficient surrogate models of thermal modeling in laser powder bed fusion, Additive Manufacturing 59 (2022) 103122. doi: https://doi.org/10.1016/j.addma.2022.103122

[33] Z. Smoqi, A. Gaikwad, B. Bevans, M.H. Kobir, J. Craig, A. Abul-Haj, A. Peralta, P. Rao, Monitoring and prediction of porosity in laser powder bed fusion using physics-informed meltpool signatures and machine learning, Journal of Materials Processing Technology 304 (2022) 117550. doi: https://doi.org/10.1016/j.jmatprotec.2022.117550

[34] F. Imani, A. Gaikwad, M. Montazeri, P. Rao, H. Yang, E. Reutzel, Process Mapping and In-Process Monitoring of Porosity in Laser Powder Bed Fusion Using Layerwise Optical Imaging, Journal of Manufacturing Science and Engineering 140(10) (2018). doi: https://doi.org/10.1115/1.4040615

[35] Q. Fang, G. Xiong, M. Zhou, T.S. Tamir, C.B. Yan, H. Wu, Z. Shen, F.Y. Wang, Process Monitoring, Diagnosis and Control of Additive Manufacturing, IEEE Transactions on Automation Science and Engineering 21(1) (2024) 1041-1067. doi: https://doi.org/10.1109/TASE.2022.3215258

[36] W. Bolton, 1 - Control systems, in: W. Bolton (Ed.), Control Systems, Newnes, Oxford, 2002, pp. 1-36.

[37] S.J. Dodds, Feedback control, Springer London 10 (2015) 978-1.

[38] R. McCann, M.A. Obeidi, C. Hughes, É. McCarthy, D.S. Egan, R.K. Vijayaraghavan, A.M. Joshi, V. Acinas Garzon, D.P. Dowling, P.J. McNally, D. Brabazon, In-situ sensing, process monitoring and machine control in Laser Powder Bed Fusion: A review, Additive Manufacturing 45 (2021) 102058. doi: https://doi.org/10.1016/j.addma.2021.102058

[39] D. Mahmoud, M. Magolon, J. Boer, M.A. Elbestawi, M.G. Mohammadi, Applications of Machine Learning in Process Monitoring and Controls of L-PBF Additive Manufacturing: A Review, Applied Sciences, 2021.

[40] R. Wang, B. Standfield, C. Dou, A.C. Law, Z.J. Kong, Real-time process monitoring and closed-loop control on laser power via a customized laser powder bed fusion platform, Additive Manufacturing 66 (2023) 103449. doi: https://doi.org/10.1016/j.addma.2023.103449

[41] V. Renken, L. Lübbert, H. Blom, A. von Freyberg, A. Fischer, Model assisted closed-loop control strategy for selective laser melting, Procedia CIRP 74 (2018) 659-663. doi: https://doi.org/10.1016/j.procir.2018.08.053

[42] M. Adnan, H.C. Yang, T.H. Kuo, F.T. Cheng, H.C. Tran, MPI-Based System 2 for Determining LPBF Process Control Thresholds and Parameters, IEEE Robotics and Automation Letters 6(4) (2021) 6553-6560. doi: https://doi.org/10.1109/LRA.2021.3092762

[43] E. Vasileska, A.G. Demir, B.M. Colosimo, B. Previtali, A novel paradigm for feedback control in LPBF: layer-wise correction for overhang structures, Advances in Manufacturing 10(2) (2022) 326-344. doi: https://doi.org/10.1007/s40436-021-00379-6

[44] B. Kavas, E.C. Balta, M. Tucker, A. Rupenyan, J. Lygeros, M. Bambach, Layer-to-layer closed-loop feedback control application for inter-layer temperature stabilization in laser powder bed fusion, Additive Manufacturing 78 (2023) 103847. doi: https://doi.org/10.1016/j.addma.2023.103847

[45] E. Malekipour, H. El-Mounayri, D. Hagedorn-Hansen, Monitoring and control framework for intelligent real-time optimization of printing sequence of powder bed fusion, Journal of Intelligent Manufacturing (2023). doi: 10.1007/s10845-023-02218-w

[46] A. Yagmur, I. Paakkonen, A. Miles, The Hitchhiker's Guide to Smart Fusion, 2023. https://www.eos.info/en-us/innovations/smart-fusion. (Accessed 7/25/2024 2023).

[47] H. Yeung, B. Lane, J. Fox, Part geometry and conduction-based laser power control for powder bed fusion additive manufacturing, Additive Manufacturing 30 (2019) 100844. doi: https://doi.org/10.1016/j.addma.2019.100844

[48] C. McCallen, ALE3D: arbitrary lagrange eulerian three-and two dimensional modeling and simulation capability, Lawrence Livemore National Laboratory, Livermore, CA (2012).

[49] Q. Wang, P. Michaleris, A.R. Nassar, J.E. Irwin, Y. Ren, C.B. Stutzman, Model-based feedforward control of laser powder bed fusion additive manufacturing, Additive Manufacturing 31 (2020) 100985. doi: https://doi.org/10.1016/j.addma.2019.100985

[50] F. Ogoke, A.B. Farimani, Thermal control of laser powder bed fusion using deep reinforcement learning, Additive Manufacturing 46 (2021) 102033. doi: https://doi.org/10.1016/j.addma.2021.102033

[51] C. He, K.S. Ramani, C.E. Okwudire, An intelligent scanning strategy (SmartScan) for improved part quality in multi-laser PBF additive manufacturing, Additive Manufacturing 64 (2023) 103427. doi: https://doi.org/10.1016/j.addma.2023.103427

[52] Z. Xi, Model Predictive Control of Melt Pool Size for the Laser Powder Bed Fusion Process Under Process Uncertainty, ASCE-ASME J Risk and Uncert in Engrg Sys Part B Mech Engrg 8(1) (2021). doi: 10.1115/1.4051746

[53] R. Yavari, R. Williams, A. Riensche, P.A. Hooper, K.D. Cole, L. Jacquemetton, H. Halliday, P.K. Rao, Thermal modeling in metal additive manufacturing using graph theory – Application to laser powder bed fusion of a large volume impeller, Additive Manufacturing 41 (2021) 101956. doi: https://doi.org/10.1016/j.addma.2021.101956

[54] V. Viale, J. Stavridis, A. Salmi, F. Bondioli, A. Saboori, Optimisation of downskin parameters to produce metallic parts via laser powder bed fusion process: an overview, The International Journal of Advanced Manufacturing Technology 123(7) (2022) 2159-2182. doi: 10.1007/s00170-022-10314-z

[55] J. Jiang, X. Xu, J. Stringer, Support Structures for Additive Manufacturing: A Review, Journal of Manufacturing and Materials Processing 2(4) (2018) 64. doi: 10.3390/jmmp2040064

[56] O. Diegel, A. Nordin, D. Motte, A Practical Guide to Design for Additive Manufacturing, Springer Series in Advanced Manufacturing (2019). doi: 10.1007/978-981-13-8281-9

[57] J.B. Coyne, John, I want to break free: The journey towards reducing or eliminating support structures in Additive Manufacturing, 2021. https://www.metal-am.com/articles/i-want-to-break-free-the-journey-towards-reducing-or-eliminating-support-structures/.

[58] M.H. Kobir, R. Yavari, A.R. Riensche, B.D. Bevans, L. Castro, K.D. Cole, P. Rao, Prediction of recoater crash in laser powder bed fusion additive manufacturing using graph theory thermomechanical modeling, Progress in Additive Manufacturing 8(3) (2023) 355-380. doi: https://doi.org/10.1007/s40964-022-00331-5

[59] K. Deshmukh, A. Riensche, B. Bevans, R.J. Lane, K. Snyder, H. Halliday, C.B. Williams, R. Mirzaeifar, P. Rao, Effect of processing parameters and thermal history on microstructure evolution and functional properties in laser powder bed fusion of 316L, Materials & Design 244 (2024) 113136. doi: https://doi.org/10.1016/j.matdes.2024.113136

[60] H. Zhang, C. Li, Q. Guo, Z. Ma, H. Li, Y. Liu, Improving creep resistance of nickel-based superalloy Inconel 718 by tailoring gamma double prime variants, Scripta Materialia 164 (2019) 66-70. doi: https://doi.org/10.1016/j.scriptamat.2019.01.041

[61] D.S. Watring, J.T. Benzing, N. Hrabe, A.D. Spear, Effects of laser-energy density and build orientation on the structure–property relationships in as-built Inconel 718 manufactured by laser powder bed fusion, Additive Manufacturing 36 (2020) 101425. doi: https://doi.org/10.1016/j.addma.2020.101425

[62] D.Q. Mayne, Model predictive control: Recent developments and future promise, Automatica 50(12) (2014) 2967-2986. doi: https://doi.org/10.1016/j.automatica.2014.10.128

[63] G. Strano, L. Hao, R.M. Everson, K.E. Evans, A new approach to the design and optimisation of support structures in additive manufacturing, The International Journal of Advanced Manufacturing Technology 66(9-12) (2013) 1247-1254. doi: 10.1007/s00170-012-4403-x

[64] A. Khobzi, F. Farhang Mehr, S. Cockcroft, D. Maijer, S.L. Sing, W.Y. Yeong, The role of block-type support structure design on the thermal field and deformation in components fabricated by Laser Powder Bed Fusion, Additive Manufacturing 51 (2022) 102644. doi: https://doi.org/10.1016/j.addma.2022.102644

[65] M. Gor, H. Soni, V. Wankhede, P. Sahlot, K. Grzelak, I. Szachgluchowicz, J. Kluczyński, A Critical Review on Effect of Process Parameters on Mechanical and Microstructural Properties of Powder-Bed Fusion Additive Manufacturing of SS316L, Materials, 2021.

[66] B. Soundararajan, D. Sofia, D. Barletta, M. Poletto, Review on modeling techniques for powder bed fusion processes based on physical principles, Additive Manufacturing 47 (2021) 102336. doi: https://doi.org/10.1016/j.addma.2021.102336

[67] B. Bevans, C. Barrett, T. Spears, A. Gaikwad, A. Riensche, Z. Smoqi, H. Halliday, P. Rao, Heterogeneous sensor data fusion for multiscale, shape agnostic flaw detection in laser powder bed fusion additive manufacturing, Virtual and Physical Prototyping 18(1) (2023). doi: https://doi.org/10.1080/17452759.2023.2196266

[68] A. Bandyopadhyay, K.D. Traxel, Invited review article: Metal-additive manufacturing—Modeling strategies for application-optimized designs, Additive Manufacturing 22 (2018) 758-774. doi: https://doi.org/10.1016/j.addma.2018.06.024

[69] Z. Luo, Y. Zhao, A survey of finite element analysis of temperature and thermal stress fields in powder bed fusion Additive Manufacturing, Additive Manufacturing 21 (2018) 318-332. doi: https://doi.org/10.1016/j.addma.2018.03.022

[70] K.D. Cole, M.R. Yavari, P.K. Rao, Computational heat transfer with spectral graph theory: Quantitative verification, International Journal of Thermal Sciences 153 (2020) 106383. doi: https://doi.org/10.1016/j.ijthermalsci.2020.106383

[71] M. Reza Yavari, R.J. Williams, K.D. Cole, P.A. Hooper, P. Rao, Thermal Modeling in Metal Additive Manufacturing Using Graph Theory: Experimental Validation With Laser Powder Bed Fusion Using In Situ Infrared Thermography Data, Journal of Manufacturing Science and Engineering 142(12) (2020). doi: https://doi.org/10.1115/1.4047619

[72] J. Ye, S.A. Khairallah, A.M. Rubenchik, M.F. Crumb, G. Guss, J. Belak, M.J. Matthews, Energy Coupling Mechanisms and Scaling Behavior Associated with Laser Powder Bed Fusion Additive Manufacturing, Advanced Engineering Materials 21(7) (2019) 1900185. doi: https://doi.org/10.1002/adem.201900185

[73] H. Peng, M. Ghasri-Khouzani, S. Gong, R. Attardo, P. Ostiguy, B.A. Gatrell, J. Budzinski, C. Tomonto, J. Neidig, M.R. Shankar, R. Billo, D.B. Go, D. Hoelzle, Fast prediction of thermal distortion in metal powder bed fusion additive manufacturing: Part 1, a thermal circuit network model, Additive Manufacturing 22 (2018) 852-868. doi: https://doi.org/10.1016/j.addma.2018.05.023

[74] D. Sarkar, A. Kapil, A. Sharma, Advances in computational modeling for laser powder bed fusion additive manufacturing: A comprehensive review of finite element techniques and strategies, Additive Manufacturing 85 (2024) 104157. doi: https://doi.org/10.1016/j.addma.2024.104157

[75] P. Wongpanya, T. Boellinghaus, G. Lothongkum, T. Kannengiesser, Effects of Preheating and Interpass Temperature on Stresses in S 1100 QL Multi-Pass Butt-Welds, Welding in the World 52(3) (2008) 79-92. doi: 10.1007/BF03266634

[76] C. Elangeswaran, A. Cutolo, S. Gallas, T.D. Dinh, N. Lammens, H. Erdelyi, M. Schulz, G.K. Muralidharan, L. Thijs, T. Craeghs, E. De Bruycker, K.V. Boer, S. Clijsters, J. Peirs, W. Desmet, W. Van Paepeghem, B. Van Hooreweder, Predicting fatigue life of metal LPBF components by combining a large fatigue database for different sample conditions with novel simulation strategies, Additive Manufacturing 50 (2022) 102570. doi: https://doi.org/10.1016/j.addma.2021.102570

Acknowledgments

Prahalada Rao acknowledges funding from the National Science Foundation (NSF) via grant numbers: CMMI-2309483/1752069, OIA-1929172, PFI-TT 2322322/2044710, CMMI-1920245, ECCS-2020246, CMMI-1739696, and CMMI-1719388; Department of the Navy, Office of Naval Research (ONR, N00014-21-1-2781) and Naval Surface Warfare Center (NAVAIR, N6833524C0215); and the National Institute of Standards and Technology (NIST) via grant 70NANB23H029T for supporting his research program.

- Understanding the causal influence of process parameters and thermal history on part quality using in-situ sensing was the major aspect of CMMI-2309483/1752069 (Program Officer: Andrew Wells).

- Commercialization of the graph theory thermal approach for ultrafast simulation of metal additive manufacturing processes is being pursued under PFI-TT 2322322/2044710 (Program Officer: Samir Iqbal).
- Preventing flaws in laser powder bed fusion through process control was funded via NIST 70NANB23H029T.

This work was made possible by the use of Virginia Tech’s Materials Characterization Facility, which is supported by the Institute for Critical Technology and Applied Science, the Macromolecules Innovation Institute, and the Office of the Vice President for Research and Innovation